A novel approach for nondestructive depth-resolved analysis of residual stress and grain interaction in the near-surface zone applied to an austenitic stainless steel sample subjected to mechanical polishing

M. Marciszko-Wiąckowska [a,*], A. Oponowicz [b], A. Baczmański [b], Ch. Braham [c], M. Wątroba [d], M. Wróbel [e], M. Klaus [f], Ch. Genzel [f]

[a] AGH-University of Science and Technology, ACMIN, al. Mickiewicza 30, 30-059 Kraków, Poland
[b] AGH-University of Science and Technology, WFiIS, al. Mickiewicza 30, 30-059 Kraków, Poland
[c] Arts et Métiers-ParisTech, PIMM, CNRS UMR 8006, 151 Bd de l'Hôpital, 75013 Paris, France
[d] EMPA, Swiss Federal Laboratories for Materials Science and Technology, Labratory for Mechanics of Materials and Nanostructures, Feuerwerkerstrasse 39, 3602 Thun, Switzerland
[e] AGH-University of Science and Technology, WIMiIP, al. Mickiewicza 30, 30-059 Kraków, Poland
[f] Abteilung fürMikrostruktur- und Eigenspannungsanalyse, Helmholtz-Zentrum Berlin fürMaterialien und Energie, Albert-Einstein-Str. 15, Berlin 12489, Germany

A B S T R A C T

The choice of the grain interaction model is a critical element of residual stress analysis using diffraction methods. For the near-surface region of a mechanically polished austenitic steel, it is shown that the application of the widely used Eshelby-Kröner model does not lead to a satisfactory agreement with experimental observations. Therefore, a new grain interaction model called 'tunable free-surface' is proposed, allowing for the determination of the in-depth evolution of the elastic interaction between grains. It has a strong physical justification and is adjusted to experimental data using three complementary verification methods. It is shown that a significant relaxation of the intergranular stresses perpendicular to the sample surface occurs in the subsurface layer having a thickness comparable with the average size of the grain. Using the new type of X-ray Stress Factors, the in-depth evolution (up to the depth of 45 μm) of residual stresses and of the strain-free lattice parameter is determined.

1. Introduction

One of the basic parameters characterizing polycrystalline material is the stress state. Stresses may exist even within a body free from external loads or temperature gradients, and such stresses are called residual stresses (RS) or locked-in stresses [1–4]. Residual stresses are summed with load-induced stresses, and they can be beneficial or detrimental to the structure, depending on whether total stresses are tensile or compressive e.g. [5–7]. Control of RS is particularly important in surface layer and coating deposition. The advantages of a subsurface stress state, usually of the compressive type, can be achieved by different treatments such as mechanical shot peening [1,8], laser shock peening/hardening [1,3,9], surface mechanical attrition treatment [2], and shot blasting [10].

In the case of polycrystalline materials, diffraction methods are commonly used in industry and research laboratories for measurement of elastic lattice deformation [11–13]. The main advantages of these methods are: their nondestructive character and, the possibility of studying the spatial distribution and anisotropy of stresses at macroscopic and microscopic scales. Another unique feature of diffraction methods is that they are phase selective, i.e. the stress can be measured independently in each phase of the material. To determine the stress in a polycrystalline material, the lattice spacings are measured along the scattering vector in different directions with respect to the sample [11,12]. The lattice strains determined from diffraction peak shifts are related to stresses using X-ray elastic constants (XEC) for non-textured materials or more generally X-ray Stress Factors (XSF) for textured samples [11,12,14]. Analysis of stress is usually done by applying the least-squares procedure or linear regression in which the stress tensor components and optionally strain-free lattice parameters are adjusted in

order to minimize the difference between measured and calculated lattice strains. A straightforward and commonly used technique is the standard X-ray $sin^2\psi$ method in which the interplanar spacings are measured with single *hkl* reflection. The principles of this methodology using Ψ or Ω-geometry are thoroughly described in handbooks concerning stress analysis [11–13]. On the basis of the measured interplanar spacings, the stress state in the so-called information depth (i.e., the depth where most of the diffracted intensity originates from)) can be studied, taking into account the first order stress, being the mean value over the studied volume, and the second order stresses describing stress deviations from the mean value for individual grains [12,15,16].

The XSF needed in stress analysis can be directly measured or determined from single crystal elastic constants and crystallographic texture using different models. The simplest and commonly used models, i.e., the Voigt [17] and Reuss [18] models for calculation of the XSF, are based on the hypothesis of strain or stress homogeneity in the considered volume, respectively [19–22]. In more advanced models, the interaction between grains is taken into account in the calculations. For example, in the Eshelby-Kröner method based on self-consistent calculations, the polycrystalline grains are approximated by an ellipsoidal inclusion embedded into a homogenous medium [14,16,23–25]. There are also models in which the direction-dependent interaction between grains is considered. The first one was proposed by Vook and Witt [26] and developed by van Leeuwen et al. [27] and Welzel et al. [14,28]. In this approach, the columnar grains, having out-of-plane dimensions equal to the thickness of the film, exhibit the same in-plane strain (a Voigt-type behavior), whereas they can deform freely in a direction perpendicular to the surface (a Reuss-type behavior). Another model, called the free-surface method, was proposed by Baczmański et al. [16]. In this approach, it was assumed that flat grains located close to the surface can freely deform in the direction normal to the surface (Reuss-type behavior), while the in-plane interaction can be approximated by the self-consistent model (Kröner-type behavior). It should be emphasized that the latter approximation describes the interaction occurring between grains penetrated by X-rays in the subsurface region where the free surface effects are significant, and it is especially suitable for the experimental techniques used in this work.

The proper choice of model for XSF calculation is a crucial point in analysis of RS and it is very important regardless of the experimental method used. Indeed, the accuracy of the obtained results depends not only on the precision of the measurement but also on the trueness of the results ultimately obtained. Even if the precision reached in the measurement is very good, the systematic error in data analysis can lead to very bad accuracy or even incorrect results. This is a case of the XSFs used to determine the stress from evaluated lattice strains. Enormous errors in stress evaluation can be the consequence of an inappropriate model used in experimental data analysis, and these become larger, the stronger the elastic anisotropy is. It is worth noting that the values of the stress calculated from the same set of lattice strain (for non-textured sample and using the standard X-ray $sin^2\psi$ method [11,12]) are 2.4 times larger for *200* reflection and 1.6 times larger for *311* and *420* reflection, comparing the results obtained with the Voigt and Reuss models, respectively. This is why in the $sin^2\psi$ method, reflections which are not very sensitive to the model assumption (e.g. *331* for austenite) are recommended for measurements, if they are available [11,12]. Unfortunately, in some cases the reflections used cannot be freely chosen, the recommended reflections are not available, or a set of different reflections must be used, as in the methodologies presented in this work for in-depth evolution of RS. Especially in such methods, special attention must be paid to the use of the proper model of XSF in order to avoid significant systematic errors in analysis of the experimental data. The main issue of the present work, which has not been considered sufficiently so far in the literature, is the study of the influence of the grain interaction model used for the calculation of the XSF for residual stress gradient analysis in the near-surface region of the materials, which is independent of the experimental method used for the stress evaluation.

The stresses in polycrystalline materials are usually inhomogeneous, therefore experimental methods allowing for the determination of their spatial distribution are particularly desirable. Experimental techniques based on neutron diffraction enable the measurements of the stress variation in large elements by scanning across the sample over distances of tens of mm with a resolution down to about one millimeter or even less (resolution is equal to the size of the gauge defined by the slip systems and/or collimators forming the incident and diffracted beam [13,29,30]). This can be done due to low absorption of neutron radiation in many materials, including metals. Also, the low absorption of high energy X-ray radiation (usually up to 100 keV or even 300 keV) allows scanning to be performed with a small gauge (typically hundreds or tens of μm, down to even 5–10 μm [9,13,31–35]) over distances typically from several up to tens or hundreds of μm in depth for the reflection mode [9,13,32,35]; or for sample thicknesses up to several mm in transmission mode [13,31,33,34]. It should be stated that the stress scanning method was developed by applying both angular dispersion (AD, [13,29,33]) and energy dispersion (ED, [31,32,34,35]) diffraction techniques. Neutron diffraction and high energy X-ray diffraction with a defined gauge are undoubtedly the most convenient methods for measurements of stress variation over mm and tens of μm, respectively. However both techniques require complex experimental data treatment when the gauge volume is not completely immersed in the sample or/and step stress gradient occurs within the gauge volume [36]. This means that the application of direct stress scanning with a predefined gauge volume is not suitable for measuring stress gradient in the subsurface region up to a few μm [9]. This is a major disadvantage because important stress gradients are often present close to the surface, especially in the case of mechanically treated materials or deposited coatings [1–3,8–10].

To study the stress gradient below the surface the destructive layer removal method is commonly used. In this method, to determine the in-depth stress profile, layers with thicknesses of several μm are removed step by step by electropolishing and the stress is measured using the standard $sin^2\psi$ X-ray method [9,12]. The in-depth resolution of the layer removal method is limited by the thickness of a layer removed in single step (usually several μm, but a thickness of 1–2 μm is reported in [9]) and the penetration depth of the X-ray radiation used (usually several μm in the case of characteristic radiation in metal samples [9,12]). Therefore, the radiation penetration depth from which the diffraction information is collected, is too large to determine the stress gradient in the range of a few micrometers. What is more, the penetration depth changes during stress measurement. The main disadvantage of layer removal namely its destructive character, cannot be overcome. It should be noted that, due to the overall stress equilibrium conditions [11], the removal of layers causes a modification of the stress state in the sample, which complicates the interpretation of the experimental data [37].

It can be concluded, that the methods presented above can be used to determine stress evolution in the sample, but also that either they are not convenient for the measurement of stress gradient very close to the surface or that they have a destructive character. This is why great effort has been made to develop a methodology which can be used to analyze the stress gradient in the subsurface region directly from diffraction results, without removing layers. In such a case the information volume is not defined by the slits but by the penetration depth of X-rays, which depends on the absorption of radiation in the studied material. Experimental techniques that are based on this approach are called Laplace methods and can be realized in different ways, e.g. using the AD or ED diffraction techniques, as it is presented in this work [32].

Two concepts of stress profile determination using a Laplace method have been developed [32]. In the first one, the penetration depth is changed during measurement and its effect on the measured lattice strains during sample tilt or rotation are analyzed in order to determine stress gradient. An example is the method based on the rotation around scattering vector (SV method), which can be applied to a strongly textured sample [38,39] or the universal plot (UP) method in which the

stress profile versus information depth (called the 'master plot') is constructed from the diffraction data obtained using different *hkl* reflections and/or wavelengths/energies in any diffraction mode [9,40,41]. These methods are rather used in special cases and require additional analysis for stress determination [32], therefore they are not suitable for application in the present work in which the elastic anisotropy and interaction between grains are considered, requiring the stress analysis method to be straightforward. It should be also mentioned that very recently the UP method has been successfully combined with the surface removal method to determine the stress evolution vs real depth *z* up to 5 μm in mechanically polished alloyed steel [9]. Thus the resolution of the layers removal technique was significantly improved and it is of about 1–2 μm. This is certainly a very interesting methodology which can be applied on a laboratory diffractometer, but it is a destructive method influencing the stress state in the sample.

Alternatively, measurements performed using Laplace methods can be made for a well-defined penetration depth which does not change during stress measurement. Then the experimental conditions are changed to study different depths and to obtain the stress vs τ profile (where τ is the information depth interpreted as the thickness of the subsurface layer from which comes 63 % of total diffraction power scattered by an infinitely thick sample [14,32], see also section 2.2). The main difficulty of such methods is to discover a way to perform measurements with different orientations of scattering vector with respect to the sample while maintaining an approximately constant information depth. To do this, different types of methods have been proposed [14,32]: (*a*) single reflection *hkl* and single wavelength AD methods, in which the sample is rotated (three rotation angles ψ, ω and φ are shown in Fig. 1b) in order to keep a constant angle between the incoming beam and the sample surface (incident angle) during stress measurement [42–44]; (*b*) multiple reflections *hkl* and the single wavelength AD method, in which many reflections for the same wavelength are measured and the incident angle is fixed during measurement [45–50]; (*c*) the single reflection *hkl* but multiple wavelengths ED method in which the appropriate values of incident angle are chosen for different radiation energies in order to maintain a constant penetration depth [51]; (*d*) multiple reflections *hkl* and multiple wavelengths ED methods, in which a combination of different radiation energies, incident angles, and reflections corresponding to the same information depth are selected [32,39,49,50,52,53].

For all the above listed methods, the information depth is constant during stress analysis and each of them is suitable for determining the stress in-depth profile at the depth of a few μm in metal samples with reasonable resolution, using energies in the range corresponding to characteristic X-ray radiations (on laboratory diffractometers or using synchrotron radiation with similar energies). Moreover, the studied depth can be significantly increased up to a dozen or tens of μm when high-energy synchrotron radiation is used (up to 90 keV). This was already demonstrated in our recent works in which the Multireflection Grazing Incidence X-ray Diffraction MGIXD method (i.e. type *b* of the approaches listed above, using CuK_α radiation on laboratory diffractometer) was combined with the Multiwavelength and Multireflection MMXD method (type *d* of the approaches listed above, using high energy synchrotron radiation) in order to measure the stress gradients produced by mechanical surface treatments for the Ti [50] and W [49] samples. In these papers, the MMXD method was proposed to measure the stress and strain-free lattice parameters (values corresponding to the material in the absence of stress) for the depth of 1–2 μm while the MGIXD method was used for the subsurface layer up to 10 – 14 μm. In the case of the Ti sample, the MGIXD and MMXD methods were applied for the hexagonal polycrystalline material (*hcp* lattice). As a result, the stress evolution as well as the in-depth changes of the a_0 as well as the a_0/c_0 strain-free lattice parameters were determined, showing a very good agreement between both methods. Also, a very good accordance between the MGIXD and MMXD methods was found for the W sample exhibiting a *bcc* crystal structure.

It should be emphasized that in the previous works [49,50], we established the methodologies which enable us to measure the biaxial stress gradient assuming a normal stress equal to zero, and what is more to determine the in-depth evolution of the strain-free lattice parameters). This, in turn, allows us to characterize the evolution in the chemical composition in the near surface region, which was, however not expected for the mechanically treated samples studied in those works (this was confirmed experimentally).

The measurements can be done in subsurface layers of metal samples up to a dozen or tens of μm including the variation of stresses very close to the surface (up to a few μm). The previously studied materials (Ti and W) exhibit minor elastic anisotropy of the single crystal elastic constants (in the case of W the Zener factor is practically equal to one), therefore all models for the calculations of XSF give very similar results. In the case of the, isotropic W sample the results are almost the same regardless of the XSF-model used. In such a case, the problem of choice of appropriate XSF-model is not important and stress analysis is straightforward.

The challenge of the present work is to develop a methodology for stress gradient determination in polycrystals with strongly anisotropic elastic properties of crystallites such as austenite (Zener factor is equal to 3.3). In such a case, the main difficulty is the significant difference between the results of the models used for calculations of the XSF. Therefore, the model as well as the type of interactions between grains must be verified before stress analysis. What is more the type of grain interaction and consequently the type of XSFs can depend on the depth below the surface due to the relaxation of the normal forces and free boundary condition of the surface. To determine properly the in-depth variation of the stresses, first of all the XSFs gradient should be determined. Moreover, the impact of the free surface on the grain interaction should be taken into account. Unfortunately, the problem of XFS

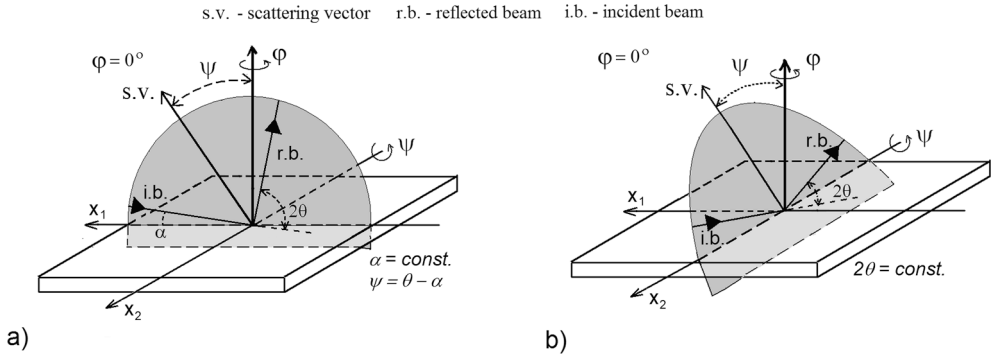

Fig. 1. Experimental geometries: a) Ω-geometry with the diffraction plane perpendicular to sample surface (for constant α angle, the ψ angle depends on the 2θ angle); b) Ψ-geometry in which the ψ angle depends on the tilt of the diffraction plane, while 2θ angle remains constant. The measurements can be performed for different φ angles.

evolution has not been thoroughly studied in the literature. The first attempt to solve this problem on the basis of the mixed Reuss-Voigt model was presented in [53]. In this paper, the gradient of XSF determined in mechanically polished austenite using different methods (including the one proposed in [53]) is presented and the physical reasons for the observed phenomena are discussed.

The methodology developed in the present work must be tested on a sample exhibiting step gradient occurring in the subsurface region at a depth of about a few μm, therefore an austenitic sample subjected to mechanical polishing was chosen. This mechanical treatment introduces a significant compressive stress very close to the surface, whose value decreases with the depth as presented in many papers [1,9,11,38,49,50]. It is worth noting that such stress is advantageous for the mechanical strength of the subsurface layer of the sample, therefore emery paper polishing is applied as the final treatment of the surface to improve the stress state at the depth of a few μm [1].

2. Methodology

The stresses can be determined by measuring lattice strains resulting from a change in the distance between planes *{hkl}* denoted by $< d(\varphi,\psi)>_{\{hkl\}}$. The measurements of $< d(\varphi,\psi)>_{\{hkl\}}$ using *hkl* reflections are performed in the direction of the scattering vector for different orientations with respect to the sample, characterized by φ and ψ angles, defined in Fig. 1. The interplanar spacings $< d(\varphi,\psi)>_{\{hkl\}}$ can be determined based on diffraction peak shift vs scattering angle 2θ (AD – angle dispersion methods) or photon energy E (ED – energy dispersion methods) [54].

The interplanar distance are determined from a well-known formulas based on Bragg's law [55]:.

for the AD methods:

$$\langle d\rangle_{\{hkl\}} = \frac{\lambda}{2\sin\theta_{hkl}}; \tag{1a}$$

and for the ED methods:

$$\langle d\rangle_{\{hkl\}} = \frac{hc}{2E_{hkl}\sin\theta}. \tag{1b}$$

where E_{hkl} and θ_{hkl} correspond to the position of *hkl* - diffraction peak on the energy scale (in ED technique) or scattering angle scale (in AD technique), h is Planck's constant, and c is the velocity of light. For the case of the ED method, the Bragg angle θ can be chosen arbitrarily, while in the AD methods the wavelength λ corresponds to the monochromatic radiation used in the experiment.

Two different measuring geometries can be chosen to change the orientation of the scattering vector. In the case of Ω-geometry, the scattering vector is inclined from the surface normal by a polar ψ angle within the diffraction plane perpendicular to the sample surface (Fig. 1a). On the other hand, in Ψ-geometry, the polar ψ angle is changed by tilting the diffraction plane relative to the sample surface (Fig. 1b). In both techniques, the azimuth angle φ is changed by rotating the sample around the surface normal. In this work, Ω-geometry is applied in the case of AD measurements (asymmetric $2\theta_{hkl}$ scan for a fixed wavelength λ), while Ψ-geometry is applied in the ED experiments (constant 2θ angle in a symmetric mode, and variable energy E_{hkl}).

2.1. Determination of the stresses from diffraction measurements

In the analysis of diffraction data obtained using the multiple reflection methods for stress determination, the normalized lattice parameters $\langle a(\varphi,\psi)\rangle_{\{hkl\}} = \langle d(\varphi,\psi)\rangle_{\{hkl\}}\sqrt{h^2+k^2+l^2}$ (for cubic crystals) are calculated and expressed as a function of the macro stress (called the first order stress [16]) σ_{ij}^I and strain-free lattice parameter a_0:

$$\langle a(\varphi,\psi)\rangle_{\{hkl\}} = \left[F_{ij}(hkl,\varphi,\psi)\sigma_{ij}^I\right]a_0 + a_0, \tag{2}$$

where $F_{ij}(hkl,\varphi,\psi)$ are the X-ray Stress Factors (XSF) [12,14,56].

Subsequently, the stress tensor components σ_{ij}^I and strain-free lattice parameter a_0 can be found using a general least-squares method or linear regression. In both approaches, the values of σ_{ij}^I and a_0 are optimized to obtain the best fit of calculated $\langle a(\varphi,\psi)\rangle_{\{hkl\}}$ lattice parameters to the experimental ones. The procedure is based on minimizing of the merit function, called the normalized χ^2, which is defined as:

$$\chi^2 = \frac{1}{N-M}\sum_{n=1}^{N}\left(\frac{\langle a(\varphi_n,\psi_n)\rangle_{\{hkl\}}^{exp} - \langle a(\varphi_n,\psi_n)\rangle_{\{hkl\}}^{cal}}{\delta_n}\right)^2, \tag{3}$$

where $\langle a(\varphi_n,\psi_n)\rangle_{\{hkl\}}^{exp}$ and $\langle a(\varphi_n,\psi_n)\rangle_{\{hkl\}}^{cal}$ are respectively the experimental and calculated lattice parameters, δ_n is the measurement uncertainty (e.g., standard deviation) of $\langle a(\varphi_n,\psi_n)\rangle_{\{hkl\}}^{exp}$ for the *n-th* measurement, and N and M are the number of measured points and fitting parameters, respectively.

In stress analysis performed in this work, the values of the lattice parameter given by Eq. (2) are fitted to experimental data using the General Linear Least Squares (GLLS) method in which the solution is obtained by applying the Singular Value Decomposition (SVD) procedure described by Press et al. [57]. The statistical uncertainties of the adjusted parameters X are calculated as the square roots from the obtained variances $Var(X)$ multiplied by χ^2, i.e.,$\delta X = \sqrt{Var(X)*\chi^2}$. Such estimation is usually made when the experimental uncertainties δ_n are unknown (but the relation between particular δ_n is known) and the so calculated uncertainties δX correspond to the assumption of a "good fit" (i.e. the assumption of such δ_n magnitudes for which $\chi^2 = 1$). The advantage of this uncertainty estimation is that the obtained δX values are determined on the basis of residuals (i.e., differences between measured and fitted $\langle a(\phi,\psi)\rangle_{\{hkl\}}$ values in Eq. (3)) and additionally the values δ_n can be used to take into account different impacts of individual measurements on the final result. Strictly speaking, the calculated uncertainties of the determined stresses and strain-free parameter (cf. Eq. (2)) are obtained from the absolute values of the residuals, but the impact of the residuals is weighted by the relation between precisions of measurements done for individual lattice parameters (expressed by $1/\delta_n$). This analysis of experimental data and statistical uncertainty is convenient when the impact of different experimental points on the final result is different, as in the case of stress analysis performed for AD methods in which different *hkl* reflections are measured for different$2\theta_{\{hkl\}}$, as discussed in section 2.2.1.

Concerning the systematic uncertainties, they can be avoided or minimized by good alignment of the experimental setup [11] and by proper choice of the XSFs used for the stress analysis (as discussed in the Introduction). Significant differences between the results of the XSF-models occur for elastically anisotropic crystallites and the effect of free surface on the values of XSFs has not been well discussed so far in the literature. Thus, the issue of the present study is to optimize the XSF-models used in analysis of stress gradient in the near-surface layers, in order to minimize the possible systematic errors and ensure the trueness of the obtained results. To do this, verifications of the methods for XSFs were performed using different grain-interaction models in which the values of $F_{ij}(hkl, \varphi, \psi, f)$ are calculated from single-crystal elastic constants taking into account crystallographic texture (f denotes the orientation distribution function ODF [58]), i.e.:

- the Voigt model assuming homogenous elastic strains for all grains independently of their orientation [17],
- the Reuss model in which the same stress is assumed for all grains [18],

M. the Eshelby-Kröner model in which stress localized in a grain is calculated on the basis of the Eshelby concept, assuming ellipsoidal inclusion embedded into a homogenous medium [23,24],

MI. the intermediate Reuss-Voigt model defined by the w – weight factor, which describes the Reuss part in the model [53], i.e.:

$$F_{ij}^{R-V} = w \cdot F_{ij}^{R} + (1-w) \cdot F_{ij}^{V}, \tag{4}$$

- a new tunable free-surface model in which the role of the free surface is taken into account in grain interactions. This model with the assumption of complete relaxation of intergranular stresses in the direction normal to a free surface was introduced by Baczmański et al. [16], while its modification is presented below.

The standard models, i.e. Reuss, Voigt and Eshelby-Kröner methods, for the calculation of XSFs are widely described in the literature (e.g. [11,12,14,16,22]), while the principles of the free-surface model are given in [16]. The principles and computation details concerning standard models are summarized in Supplementary Data.

2.1.1. New tunable free-surface model

The idea of different grain interactions in different directions with respect to the free surface was previously proposed in the Vook – Witt (or inverse Vook – Witt) model, in which the Voigt-type of iteration in the surface plane and the Reuss-type interaction in normal direction were assumed (or inverse assumptions in the inverse model) [14,28]. Subsequently, a more physically reasonable free-surface model was proposed by introducing the assumption of the Eshelby-Kröner interaction in the free surface plane and Reuss-type interaction in the normal direction [16].

Following the above ideas, we introduce the tunable free-surface model in which the stress concentration tensor B_{ijkl}^{F-s} relating macrostress (σ_{kl}^{I}) to the stress localized in a grain (σ_{ij}^{g}) is defined [16]:

$$\sigma_{ij}^{g} = B_{ijkl}^{F-s} \sigma_{kl}^{I}. \tag{5}$$

The B_{ijkl}^{F-s} tensor is determined from an analogical tensor B_{ijkl}^{E-K} calculated using the self-consistent calculation for ellipsoidal inclusion embedded in a mean matrix, i.e.:

$$B_{ijkl}^{F-s} = \begin{cases} r \cdot I_{ijkl} + (1-r) \cdot B_{ijkl}^{E-K} & \text{for i} = 3 \text{ or j} = 3 \\ B_{ijkl}^{E-K} & \text{for i} \neq 3 \text{ and j} \neq 3 \end{cases} \tag{6}$$

where I_{ijkl} is the identity tensor, and B_{ijkl}^{E-K} is the concentration tensor calculated for an inclusion completely embedded in the material. At the same time, r represents a degree of intergranular stresses relaxation in the direction normal to the surface (see that for $r = 1$ the Reuss model is assumed for the intergranuler stresses perpendicular to the surface).

The procedure of B_{ijkl}^{E-K} calculation and determination of F_{ij}^{F-s} stress factors (from B_{ijkl}^{F-s} tensor) taking into account crystallographic texture is described in Supplementary Data and in [16].

2.1.2. Assessments of X-ray stress factors

The models for XSF prediction are verified using three different criteria. The most objective method for model verification is based on a direct comparison of the measured XSFs with the predicted ones. The lattice strains are measured '*in-situ*' under a known load applied to the sample. In order to avoid the influence of unknown residual stresses or/and systematic errors of diffraction peak position determination, measurements for the non-loaded sample and a sample under uniaxial stress are used to determine relative lattice strain [21,59,60]. The so determined elastic response of the lattice to the applied residual or applied stress σ_{ij}^{I} can be used to determine the values of XSFs experimentally. For example, if a known uniaxial stress σ_{11}^{I} is applied to the sample, the factor $F_{11}(hkl, \varphi, \psi, f)$ can be calculated from the corresponding lattice strain $< \varepsilon(\varphi,\psi) >_{\{hkl\}}^{e}$, measured as the change in the interplanar spacings:

$$F_{11}(hkl, \varphi, \psi, f) = \frac{\partial < \varepsilon(\varphi,\psi) >_{\{hkl\}}^{e}}{\partial \sigma_{11}^{I}} = \frac{< d(\varphi,\psi) >_{\{hkl\}}^{\sigma} - < d(\varphi,\psi) >_{\{hkl\}}^{0}}{< d(\varphi,\psi) >_{\{hkl\}}^{0} \sigma_{11}^{I}}, \tag{7}$$

where $< d(\varphi,\psi) >_{\{hkl\}}^{\sigma}$ and $< d(\varphi,\psi) >_{\{hkl\}}^{0}$ are the interplanar spacings for the sample under applied load and unloaded sample, respectively; and f means dependence of F_{11} on ODF for the textured sample.

Using the above formula, the XFSs can be measured and subsequently the model $F_{11}^{mod}(hkl, \varphi, \psi, f)$ can be compared with the experimental ones $F_{11}^{exp}(hkl, \varphi, \psi, f)$. The qualitative parameter of convergence of both results can be defined:

$$\delta^2 = \sum_{n=1}^{N} \left(F_{11}^{exp}(hkl, \varphi, \psi, f) - F_{11}^{mod}(hkl, \varphi, \psi, f) \right)^2. \tag{8}$$

It should be underlined that in the above method, the influence of such effects as the influence of stacking faults [59] or plastic incompatibility stresses [22,61] on the determined XSFs is significantly reduced since the effect of stress σ_{ij}^{I} on the lattice strain, defined in Eq. 1, is exclusively taken into account.

Another verification of the XSFs can be done by analyzing the results of residual stress measurements. In such a case, the quality of matching theoretical values of lattice parameters to the measured ones is examined for different models of XSFs. Assuming that the effect of the σ_{ij}^{I} on the measured $< a(\varphi,\psi) >_{\{hkl\}}^{\sigma}$ is dominant (i.e., the plastic incompatibilities are not significant and the influence of stacking faults is negligible), the values of the first order stresses σ_{ij}^{I} and value of the strain-free parameter a_0 can be determined using the least-squares method based on Eq. (2). The obtained minimum value of χ^2 (Eq. (3)) can be considered the model correctness measure. The values of this parameter can be compared for different XSF-models, searching for the best one with the smallest χ^2.

A third way of XSF verification is described in [53], and it is based on the analysis of the in-depth gradient of residual stress. This method is applied for the so-called Laplace space method of stress evolution measurement for gauge volumes defined by the information depth of the used radiation (for details, see, e.g. [53]). The refinement strategy is based on the assumption that the residual stress depth profiles in the Laplace space should be smooth with minimal jumps between neighboring points $\sigma_{ij}^{I}(\tau_n)$ measured using different reflections *hkl*. As discussed in [53], the shape of the residual stress depth profiles varies significantly for the different XSF-models. This behavior is due to the elastic anisotropy of the crystallites of which the material is composed. A measure to describe the smoothness of the residual stress depth profiles given in discrete points τ_n is the total path length of the joins between two neighboring data points Σ_Δ [53]:

$$\Sigma_\Delta^2 = \sum_{n=1}^{N-1} \left(\left[\Delta \sigma_{ij}^{I}(\tau_n) \right]^2 + [\Delta \tau_n]^2 \right), \tag{9}$$

where $\Delta \sigma_{ij}^{I}(\tau_n) = \sigma_{ij}^{I}(\tau_{n+1}) - \sigma_{ij}^{I}(\tau_n)$ and $\Delta \tau_n = \tau_{n+1} - \tau_n$ are calculated for two neighboring data points, while N is the number of information depths τ_n for which the stresses were measured.

The smallest value of Σ_Δ^2 determines the best XSF-model.

2.2. Laplace space methods

The difference between methods using a gauge volume and the Laplace space method for the determination of the stress gradient below the sample surface is shown in Fig. 2. Scanning with a gauge volume

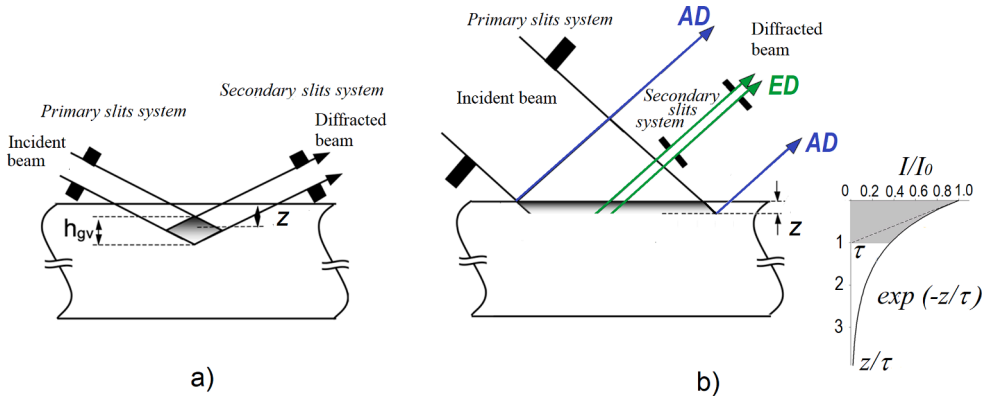

Fig. 2. Different modes of X-ray diffraction used to measure stress gradient below the surface: (a) the narrow-slit configuration with small gauge (h_{gv} is the high of the gauge immersed in the sample at depth z) and (b) wide-slit configurations (AD-angular dispersion and ED-energy dispersion) for which information depth τ is defined by Eq. (10). In the Laplace method (b), the beam intensity variation with depth z below the surface is presented.

(Fig. 2a) is performed vs real depth (z) with resolution limited by the gauge heighth_{gv}. In the case of the Laplace method, the measured X-ray signal is assigned to an average information depthτ, which is defined as a position of 'centroid' or 'weighted average' of the diffraction power contributing to a given reflection, i.e.:

$$\tau = \int_0^\infty z \cdot dP(z) \Big/ \int_0^\infty dP(z) = \int_0^\infty z \cdot \exp(-\mu k z) dz \Big/ \int_0^\infty \exp(-\mu k z) dz = (\mu k)^{-1}, \quad (10)$$

where $dP(z)$ is the diffraction power of radiation scattered at the depth z (see Fig. 2b) by a thin layer having a thickness dz, k – geometry factor relating the geometrical path of the X-ray beam within the sample to the depth z, and μ is the linear absorption coefficient for the radiation used and the studied material.

It should be emphasized that the main disadvantage of the Laplace method is that the lattice strain/stress is determined as a function of information depth τ, while in the case of defined gauge the scanning is done directly as a function of real depth z. To obtain the stress profile vs depth z the stress vs τ function must be transformed using the inverse Laplace transform [42,62], which is also used in the present paper. This transformation is not always easy and requires additional assumptions concerning stress profile. However, the Laplace space methods are the only ones that can be used to determine nondestructively the stress profile in polycrystalline materials (e.g. metals) for depths of a few μm.

In the case of the Laplace space method, the choice of the measurement geometry and energy of radiation used, in general, depends on the material and the range of investigated depth; however, the data treatment strategy is also crucial. In the present work, two Laplace space techniques (ED and AD [48–50,63]) were applied to measure the residual stress distribution in the near-surface layers, and different ways of interpreting the results were compared.

The Laplace space methods used in this work and different data analysis strategies are presented in this section and shortly summarized in Table 1. In the calculations carried out using all the presented methods, a biaxial stress state was assumed with the main axes coinciding with the axes of the sample reference system (i.e. $\sigma^I_{33} = 0$ and all first order shear stresses are neglected). This assumption is reasonable in the case of nondirectional polishing which should create stresses having rotational in-plane symmetry of the stresses. In this case the macroscopic residual shear stresses are negligible, in contrast to the one directional mechanical treatment like for example grinding for which the σ^I_{i3} RS are generated [11,12]. The rotational in-plane symmetry can be confirmed through determination of the independent stress tensor components σ^I_{11} and σ^I_{22} and verification if $\sigma^I_{11} = \sigma^I_{22}$.

Table 1
Classification of the Laplace space method used in this work.

The technique of interplanar spacing determination	AD – angle dispersive mode	ED – energy dispersive mode
Geometry of measurements/ method of analysis	Ω - geometry (Fig. 1a)/ MGIXD – multireflection grazing incidence diffraction	Ψ - geometry (Fig. 1b)/ MMWP - modified multi-wavelength plot MMXD -multireflection and multi-wavelength X-ray diffraction

2.2.1. MGIXD – Angle dispersive method

The first AD – method applied in this work is the MGIXD [47,50,64,65], introduced as Low Incidence Beam Angle Diffraction (LIBAD [45]). In this method, the measurements are performed with a monochromatic wavelength (i.e., characteristic radiation on a laboratory diffractometer), for several *hkl* reflections. The measurements are done using the Ω geometry (cf. Fig. 1a) for an approximately constant information depth when a small angle of incidence (α) is fixed for the incoming beam.

During measurement, the normalized lattice parameter $\langle a(\phi,\psi)\rangle_{\{hkl\}}$ is determined for different inclinations ψ_{hkl} of the scattering vector from normal direction (Fig. 1a), which are related to a constant incident angle α and different diffraction angles $2\theta_{hkl}$ corresponding to available experimentally *hkl* reflections, i.e.:

$$\psi_{hkl} = \theta_{hkl} - \alpha, \quad (11)$$

where the scattering angle $2\theta_{hkl}$, the incident angle α and the polar angle ψ_{hkl} are defined in Fig. 1a.

To determine the biaxial stress state, measurements should be done for two different azimuthal angles φ (Fig. 1a). The information depth τ (defined by Eq. (10)) can be changed systematically by setting different α angles [65]. It can be shown that the information depth τ can be calculated from the formula:

$$\tau = (k\mu)^{-1} = \left(\frac{1}{\sin\alpha} + \frac{1}{\sin(2\theta_{hkl} - \alpha)}\right)^{-1} \mu^{-1}, \quad (12)$$

where μ is the linear absorption coefficient of X-rays for a given energy of radiation.

As illustrated in Fig. 3, which was drawn according to Eq. (12), the penetration depth τ is approximately constant for a given value of the incident angle α and radiation used (within the range indicated in Table 2), despite different values of ψ angles chosen for the measurements. On the other hand, the depth τ significantly varies when the value of α or the energy of radiation is changed.

In analysis of the of experimental results and calculation of statistical

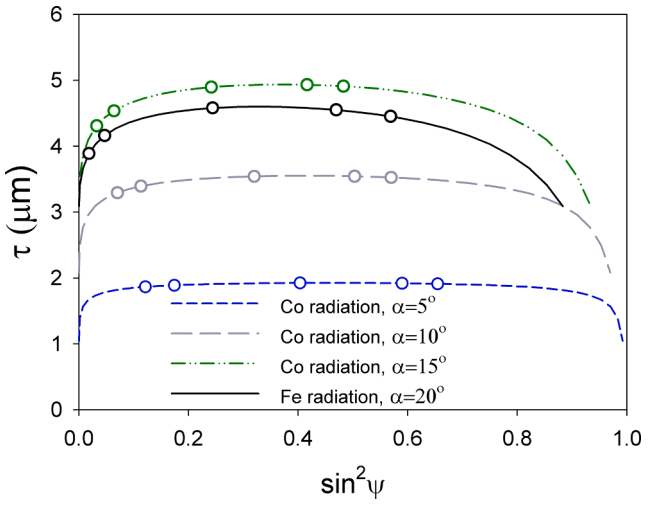

Fig. 3. Penetration depth τ in function of $sin^2\psi$calculated from Eq. (12) for austenitic steel and two radiations used: Fe $K_{\alpha 1}$ radiation (linear attenuation coefficient $\mu = 554$ cm^{-1}) and Cu $K_{\alpha 1}$ radiation ($\mu = 417$ cm^{-1}). The lines for different incident angles α are presented, while the points represent orientations for which the diffraction measurements were done.

Table 2
The mean information depths and the corresponding tolerance ranges chosen for measurements using MGIXD and MMXD methods.

Method	Information depth τ and the tolerance range (μm)			
MGIXD	1.90 (1.87–1.92)*	3.46 (3.29–3.54)*	4.72 (4.31–4.93)*	4.33 (3.89–4.57)**
MMXD	3 ± 1	8 ± 4	18 ± 6	30 ± 5

* Co radiation ** Fe radiation

uncertainty, the GLLS -SVD procedure described in section 2.1 was used. As mentioned, in the case of the AD multiple reflection method, the impact of the measured lattice parameters on the determined stresses should be weighted accounting for the propagation of the uncertainty according to the formula:

$$\delta_n = \sqrt{h^2 + k^2 + l^2}\ cot\ \theta_{hkl}\ \delta_{2\theta_{hkl}}, \tag{13}$$

where $\delta_{2\theta_{hkl}}$ is the uncertainty of the measured $2\theta_{hkl}$, i.e. the position of the determined diffraction peak, and δ_n is the uncertainty of the lattice parameter which should be substituted into Eq. (3).

It should be emphasized that due to the $cot\theta_{\{hkl\}}$ multiplier in Eq. (13), so defined uncertainties δ_n are much lower for a higher $2\theta_{hkl}$ angle. Because the inverse of squared uncertainties plays the role of weight in the merit function χ^2 (Eq. (3)), the values of $\langle a(\varphi,\psi)\rangle_{\{hkl\}}$ measured with higher $2\theta_{hkl}$ angles influence much more strongly the finally determined values of stresses and the a_0 lattice parameter.

Our previous experiments performed with samples under external loading $2\theta_{hkl}$ [57,58] as well as for powder samples show that the uncertainties of peak positions $\delta_{2\theta_{hkl}}$ (given by diffraction peak fitting with a pseudo-Voigt function [66]) are seriously underestimated in comparison with the spread observed for the experimental points this is due to unknown instrumental errors, the influence of microstresses, stress heterogeneity and many unknown reasons which are difficult to estimate. This is why the uncertainty analysis with the assumption of a 'good fit', based on the residuals and the relation between the δ_n is the most reasonable. In the case of analysis performed for data obtained with the MGIXD method, a constant value of $\delta_{2\theta_{hkl}} = 0.01^\circ$ is assumed, approximately mimicking the length of the error bar compared with the residuals in our previous test [57,58] and also given by Hauk [12] in the case of standard X-ray measurement. In the estimation performed for the experimental data the assumed value of $\delta_{2\theta_{hkl}}$ does not influence the calculated stresses and strain-free parameter or their uncertainties, while the relation between δ_n for particular measured peak positions is given by the Eq. (13), which reflects the much stronger propagation of statistical errors for lower values of scattering angle $2\theta_{hkl}$.

2.2.2. *MMWP and MMXD – Energy dispersive methods*

The second method based on Laplace space used in this work is the ED – MMWP (energy dispersive – modified multi-wavelength plot), in which a white synchrotron X-ray beam is used [39,54,67]. The ED method provides complete diffraction patterns with a multitude of *hkl* diffraction lines, which are obtained for a given orientation (φ,ψ) of the scattering vector at a fixed diffraction angle 2θ. The relationship between the interplanar distance and the energy of the diffraction line is given by Eq. 1, in which θ angle remains constant during measurements. It should be underlined that the information depth depends on the energy of the diffraction line. Therefore, the information depth is different for various *hkl* reflections when the ψ and θ angles remain constant.

Determination of residual stresses is based on the measurement of interplanar spacings for different orientations of the scattering vector. Therefore, the ψ and φ angles have to be changed. It can be shown that for the ED mode with a constant 2θ angle (experimental geometry presented in Fig. 1b), the information depth τ depends both on the energy for which the *hkl* reflection is measured, as well as on the polar angle ψ, i.e.:

$$\tau = (k\mu)^{-1} = \left(\frac{\sin\theta\cdot\cos\psi}{2}\right)(\mu_{E_{hkl}})^{-1}, \tag{14}$$

where $\mu_{E_{hkl}}$ is the energy-dependent linear absorption coefficient.

A unique advantage of the ED –MMWP method used with high-energy X-rays is the possibility of stress measurements for much deeper layers than the AD-MGIXD method, for which characteristic X-ray series are used on a laboratory diffractometer. On the other hand, the presented MGIXD method enables measurement close to the surface. Therefore, both techniques are complementary.

As mentioned above, in the case of the ED – MMWP method the information depth depends both on the orientation of the scattering vector (ψ – angle) and *hkl* reflection (E_{hkl}). To prevent τ variation during measurement of stresses for the chosen information depth, different strategies of data treatment were proposed and tested [49,50,53].

Near-surface residual stress analysis performed in the ED diffraction mode provides depth profiles for the in-plane normal and the out-of-plane shear stress components, σ_{ii}^I and $\sigma_{i3}^I (i = 1,2)$, respectively. They are obtained by applying $\sin^2\psi$-based data evaluation techniques [5] to each *hkl* diffraction line in the ED diffraction spectra, which have to be recorded for various inclination anglesψ. In this way, even steep stress gradients can be analyzed, if only data up to $\psi \approx 45^\circ$ ($\sin^2\psi = 0.5$) are taken into account in the evaluation. In [53], it was shown theoretically that the $\langle a(\varphi,\psi)\rangle_{\{hkl\}}$ vs $\sin^2\psi$ – distributions remain nearly linear within this range even in the case of strongly varying stress fields if two conditions are fulfilled (as for the studied in this work sample), i.e., severe plastic deformation leading to *hkl*-depended nonlinearities in the $\sin^2\psi$ plots is excluded and the material features weak crystallographic texture, i.e. the elastic anisotropy is restricted to the microscopic (crystallite) scale. Then, even steep residual stress depth gradients result in $\sin^2\psi$ distributions with a *hkl* dependent slope (elastic anisotropy), which remain almost linear up to large ψ -angles. This allows to take the linear parts of the $\sin^2\psi$ plot, in order to calculate the stress values from the slope of the regression line (if the plot is still linear above $\sin^2\psi = 0.5$, the range used for regression can be extended, e.g. up to 0.8 as in the present work). Plotting the residual stress values for each component σ_{ij} obtained for the individual reflections *hkl* versus the maximum information depths $\tau_0^{hkl} = \tau^{hkl}(\psi = 0)$ (cf. Eq. (14)), yields discrete stress depth distributions in the Laplace space, i.e. $\sigma_{ij}(\tau)$.

Another way of data treatment applied for data obtained with ED technique is the MMXD method [49,50]. The analysis is based on the selection of $\langle a(\varphi,\psi)\rangle_{\{hkl\}}$ values measured for different ψ andE_{hkl}, but corresponding approximately (with a chosen tolerance) to the same information depth τ (defined by Eq. (14)). This way, the data for a wide range of angle ψ (or $sin^2\psi$) can be collected when different *hkl* reflections are taken into account simultaneously. The information depths and their ranges chosen in this work are given in Table 2.

Further analysis applied for the MMWP and MMXD methods is similar to that applied in the case of the AD - MGIXD method, and the experimental uncertainties are taken into account in the calculation of the merit function χ^2 in Eq. (3). To determine the stress tensor components σ_{ij} and strain-free lattice parameter a_0, the least-squares procedure GLLS -SVD described in section 2.1 is used. However, in this case the interplanar spacings and their uncertainties δ_n were directly obtained from the ED spectra, so the formula for propagation of the uncertainty (Eq. (13)) was not used, and all measurements were done for the same angle $2\theta = 16^\circ$.

2.3. Determination of stress profile versus real depth

The results of the above described Laplace space methods are obtained in the Laplace space (i.e. as a function of τ) and can be transformed back into the real or z-space, in order to obtain the actual profiles,$\sigma_{ij}(z)$. Due to Beer's exponential attenuation law, the experimentally accessible stress depth profiles $\sigma_{ij}(\tau)$ are the Laplace transforms of the actual (real or z-space) profiles $\sigma_{ij}(z)$ with respect to the inverse of the information depth τ (given by the Eqs. (12) or (14)):.

$$\sigma_{ij}(\tau) = \frac{\int_0^\infty e^{-\frac{z}{\tau}}\sigma_{ij}(z)dz}{\int_0^\infty e^{-\frac{z}{\tau}}dz} = \frac{1}{\tau}\, L\left[\sigma_{ij}(z);\frac{1}{\tau}\right], \tag{15}$$

where z is a "real depth" under the sample surface, while τ is the information depth.

The way to obtain discrete $\sigma_{ij}(\tau)$ profiles from the measured lattice spacing depth profiles $\langle a(\varphi,\psi)\rangle_{\{hkl\}}(\tau)$ by means of Eq. (2) depends on the microstructure and composition in the near surface zone of the material. If gradients of the strain-free lattice parameter a_0 and of the XSF can be excluded, the so-called 'variable depth methods' based on Eq. (14) (cf. Fig. 1b) can be applied [32]. On the other hand, $a_0(z)$ gradients and/or gradients of the XSF (topic of this paper), which superimpose the stress gradients, require the application of the 'constant depth methods' based on Eq. (12) (cf. Fig. 1a) [45,47]. Regardless of the method used, it has proven useful for calculating the $\sigma_{ij}(z)$ profiles to describe them by exponentially damped polynomial functions whose Laplace transforms (see Eq. (15)) are fitted to the discrete $\sigma_{ij}(\tau)$ distributions by means of a least-squares fit.

Since the XSF gradient is investigated in this paper, the stresses $\sigma_{ij}(\tau)$ should be determined for given information depths τ, which must be approximately constant during measurement of interplanar spacings $\langle d(\varphi,\psi)\rangle_{\{hkl\}}$. This condition is usually fulfilled in a good approximation for MGIXD, as shown in Fig. 3 and Table 2. However, in the case of ED methods, the penetration depth given by Eq. (14) significantly changes for different ψ angles used in the experiment (analysis of such results can potentially lead to errors in the case of significant stress gradients [68]).

This is a reason of the method modifications in order to take into account in analysis only those lattice strain measurements for which the information depth does not change significantly, i.e. the appropriate choice of ψ angles of different *hkl* reflections in MMXD analysis or reduction of ψ range in the MMWP method. Finally, the considered ranges of assumed depth must be verified, taking into account the stress gradient determined in the sample.

The mean information depths τ and the deviations from these values (ranges) for which the stress were determined usingthe MGIXD and MMXD methods are shown in Table 2.

3. Experimental

3.1. Material

An austenitic stainless steel AISI 316L with the fcc structure and chemical composition given in Table 3 was investigated in our previous work [59] and in the present study. All samples studied were machined from the same hot rolled sheet having a thickness of 3 mm. The single-crystal elastic constants (C_{ij}) for austenite collected in Table 4 indicate the relatively high elastic anisotropy of the crystallites (i.e., the Zener ratio is equal to 3.3) [69].

Electron backscattered diffraction inverse pole figure maps (EBSD-IPF), together with the studied sample's crystallographic texture, are presented in Fig. 4. An EBSD analysis was performed near the surface on two perpendicular planes using an FEI Versa 3D field emission scanning electron microscope equipped with a Symmetry S2 EBSD detector from Oxford Instruments. The EBSD map size and step size were set to 600 μm × 400 μm and 400 nm, respectively. The Kikuchi pattern identification fraction exceeded 96.6 % in both maps. Grains were defined by a set of at least 15 measurement points surrounded by a continuous grain boundary segment with a misorientation of at least 5°. Fig. 4a presents a uniform, microstructure with approximately equiaxed grains (containing recrystallization twins) with a mean size of 8 μm. The crystallographic texture was characterized by the X-ray diffraction method using Co radiation and the calculated ODF, presenting relatively low texture intensities (Fig. 4b).

The samples prepared for stress profile analysis with MGIXD, MMWP and MMXD methods were non-directionally mechanically polished using 2400 grit abrasive paper. The average roughness of the prepared sample was R_a = 482 nm, determined using an optical profiler (Veeco WYKO NT 930).

3.2. Diffraction measurements

The stress measurements were performed using the Panalytical Empyrean diffractometer (AD- MGIXD method [47,49,50,60]) and then applying the high-energy synchrotron energy-dispersive diffraction (ED – MMWP method [49,50,53]) at the EDDI@BESSYII beamline (HZB, Berlin) [41]. A grazing incident experiment using Fe radiation ($K_{\alpha1}$ = 1.936 Å and $K_{\alpha2}$ = 1.940 Å) in the reflection mode during an '*in-situ*' tensile test (Fig. 5a) was performed previously (details are given in [59]). The experimental data obtained in this experiment are used in the present work to determine XSF close to the sample surface.

In the case of '*in-situ*' measurements in transmission mode, a new experiment with high energy synchrotron radiation (8….120 keV) was performed (Fig. 5b) for a bone-shaped sample with a gauge dimension of 15 mm × 5 mm × 3 mm (the beam passed through the sample at a thickness equal to 3 mm).

The residual stress in mechanically polished sample were measured (Fig. 1a and 3a) on the classical diffractometer, using Co radiation ($K_{\alpha1}$ = 1.789 Å and $K_{\alpha2}$ = 1.793 Å) and Fe radiation in the reflection mode. Both lines $K_{\alpha1}$ and $K_{\alpha2}$ were fitted simultaneously by the pseudo-Voigt function in order to determine double-peak position vs $2\theta_{hkl}$ angle [66]. Measurements were performed in parallel beam geometry. The incident beam optic was equipped with a Göbel mirror and Soller slit (2.29°) with a fixed divergence slit (1/2°), whereas the diffracted beam optic was equipped with a parallel plate collimator (0.18°) and Soller slit (2.29°). The MGIXD method (cf. Fig. 1 a) was applied for three incident angles α: 5°, 10°, 15° and for φ = 0°, 90°. LaB_6 powder was used to eliminate apparatus misalignment errors.

The energy-dispersive method with a white X-ray beam (wavelength in the range λ: 0.3–0.18 Å) was used for the synchrotron measurements in the reflection (Fig. 1b) and transmission modes (Fig. 3b). In the reflection mode, the primary beam cross-section was equal to 0.5 × 0.5 mm^2, and the angular divergence in the diffracted beam was restricted by a double-slit system with apertures of 0.03 × 5 mm^2 to $\Delta\theta \leq 0.005^\circ$.

Table 3
Composition of austenitic stainless steel (wt.%).

Fe bal.	Cr 17.24	Ni 11.14	Mo 1.96	Mn 1.67	Cu 0.35	Si 0.056	P 0.04	S 0.04	C 0.02

Table 4
Single-crystal elastic constants C_{ij} for studied austenitic stainless steel.

C_{11} (GPa)	C_{12} (GPa)	C_{44} (GPa)	Zener factor
197	122	124	3.3

Diffractograms in the form of intensity vs photon energy E_{hkl} were collected in the symmetrical Ψ-mode ° (cf. Fig. 1b) with steps of $\Delta\psi = 4°$ in the range $\psi = (0°; 72°)$. The measurements were done for azimuth angles φ: 0° and 90°, and for a chosen scattering angle $2\theta = 16°$.

In the transmission mode (Fig. 3b), the primary beam cross-section was equal to 1 × 1 mm^2, and the angular divergence in the diffracted beam was restricted by a double-slit system with apertures of 0.1 × 5 mm^2. Diffractograms were collected in the symmetrical transmission mode for a $2\theta = 23.4°$ scattering angle with equal steps of 0.1 vs $cos^2\varphi$ in the range $\varphi = (0°; 90°)$.

For both modes of synchrotron measurements, the interplanar spacings $\langle d(\varphi,\psi)\rangle_{\{hkl\}}$ were evaluated using Eq. 1 for various diffraction line positions (E_{hkl}) that were determined by fitting the pseudo-Voigt function to the measured diffraction peaks [66]. Au powder was used to correct geometrical errors due to apparatus misalignment.

4. Results

4.1. Analysis of X-ray stress factors

As mentioned above to avoid or minimize systematic errors in stress analysis at first the verification of XSF-model must be done and the

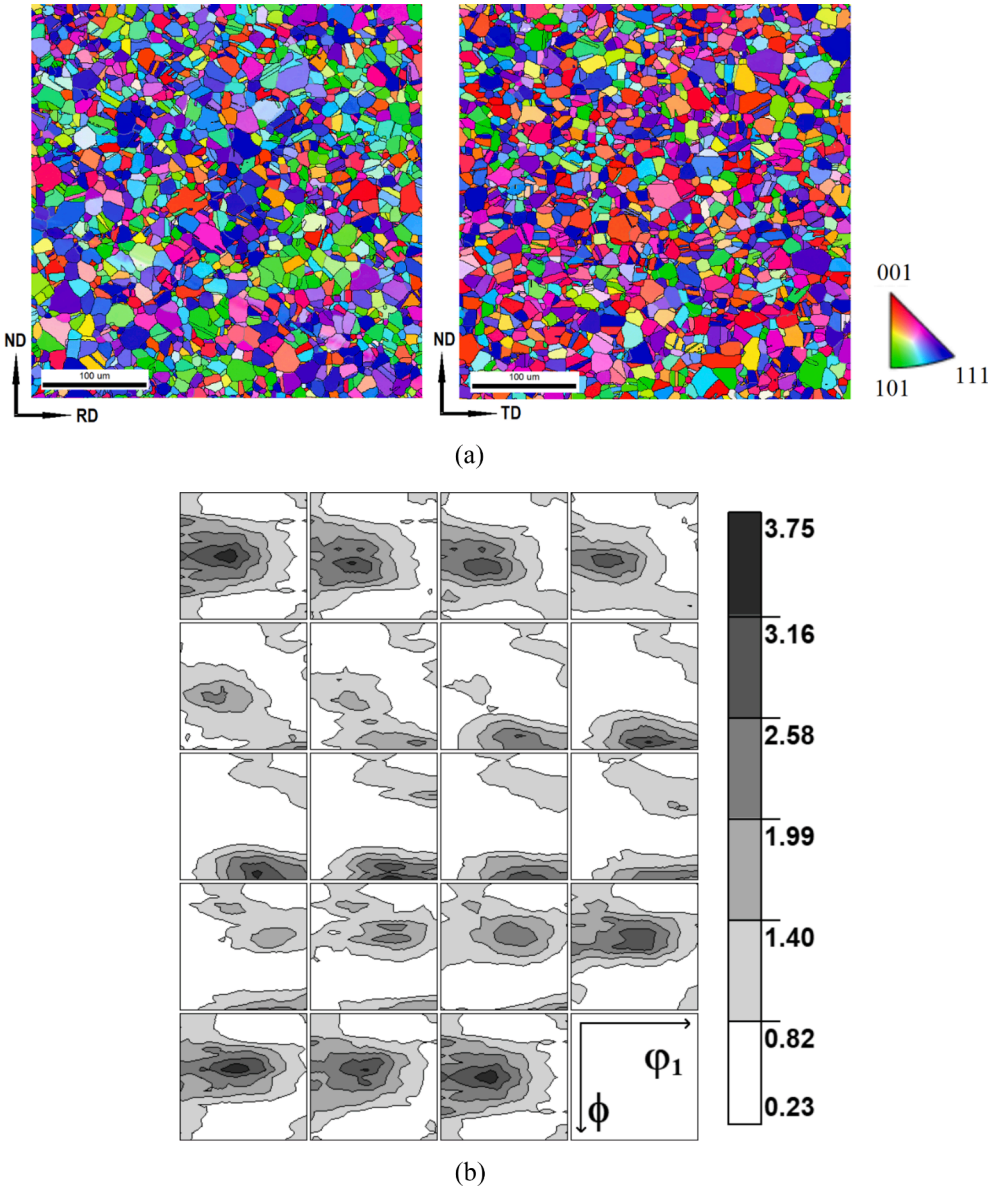

Fig. 4. EBSD (a) orientation map (colors show orientations of the normal to the sample surface with respect to the crystal frame). Orientation distribution function (ODF) (b) determined using Co radiation. The sections through Euler space with the step of 5° are presented along the axis ϕ_2.

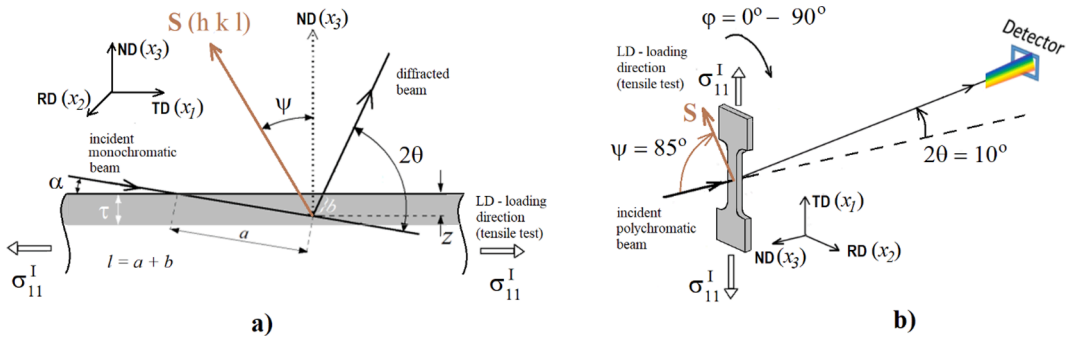

Fig.5. Experimental geometries used for in-situ diffraction measurements with applied external load; a) reflection (MGIXD – Co radiation) and b) transmission (high energy synchrotron diffraction).

evolution of XSFs with depth below the surface should be determined. To do this, different models were applied in which the calculations of the XSFs were performed for a set of 200 grains having different orientations with respect to the sample described statistically by the ODF presented in Fig. 4b. The single-crystal elastic constants given in Table 4 [69] were used for each grain, accounting for its orientation.

4.1.1. XSF verification based on lattice strains under applied loads

The experimental values of XSF were calculated on the basis of the measurements performed in our previous work [59] in which the lattice strains were measured '*in-situ*' during uniaxial tensile loading and unloading of the sample, in the elastic range of deformation. The measurements were done using MGIXD method for an information depth τ = 4.33 μm corresponding to Kα - Fe radiation and an incident angle α = 20° (Fig. 5a). In Fig. 6, the determined lattice parameters $\langle a(\varphi,\psi)\rangle_{\{hkl\}}$ vs $sin^2\psi$ measured for two angles and $\varphi = 0°$ and 90°, are shown for three states of the sample: initial, under load for which $\sigma^I_{11} = 300$ MPa, and unloaded. It was found that after loading to maximal load ($\sigma^I_{11} = 300$ MPa) and complete unloading, the values of interplanar spacings were not changed significantly, i.e. the sample returned to the initial state. In the initial and unloaded states small nonlinearities and slopes of the $\langle a(\varphi,\psi)\rangle_{\{hkl\}}$ vs $sin^2\psi$ plots are observed (cf. Fig. 6). To determine the relative strains, the measured interplanar spacings for the initial sample were subtracted from those measured under applied loads. Therefore, the effects of small second order plastic incompatibility stresses and/or possible stacking faults are avoided when the XSFs are calculated.

The comparison between experimental F^{exp}_{ii} (points) and model F^{mod}_{ii} (lines) XSFs is shown in Fig. 7 for different *hkl* reflections, and $\varphi = 0°$ and 90°. The experimental data were determined from MGIXD measurements with an applied uniaxial load corresponding to stress $\sigma^I_{11} = 300$ MPa. In these figures, the experimental bar corresponding to the $2\theta_{hkl}$ peak position uncertainty is shown illustrating different propagation of the uncertainty for different angles $2\theta_{hkl}$. It should be stated that this value error estimation is probably overestimated because uncertainties such as misalignments of the diffractometer and inaccuracy of sample position are canceled when the relative lattice strains are calculated. It is clearly seen that the nonlinearities of the F^{exp}_{ii} vs $sin^2\psi$ plots significantly exceed the error bars, even forthe smallest values of angle $2\theta_{hkl}$.

The verification of the model for XSF calculation was based on a direct comparison of experimental F^{exp}_{ii} and model F^{mod}_{ii} factors determined for the three loads corresponding to macroscopic stresses of 180 MPa, 300 MPa during loading and 180 MPa during unloading of the sample. The models' optimizations were based on a minimization of the δ^2 parameter, given by Eq. (8), and the obtained results are presented in Fig. S3 (Supplementary Data) and comprised in Table 5. The best agreement between experimental and theoretical data was found for the intermediate Reuss-Voigt model with a mean value $w = 0.76$ (Eq. 4), and the tunable free-surface model with $r = 0.74$ (Eq. (6)), corresponding to a significant relaxation of intergranular stresses in the direction normal to the surface (i.e. $\sigma^g_{i3} \to \sigma^I_{i3} \to 0$ for $i = 1,2,3$). In both cases, the mean values were calculated for three applied loads. The worst agreement was obtained for Voigt (i.e. $w = 0$ in Eq. 4) and Eshelby-Kröner (i.e. $r = 0$ in Eq. (6)).

A second comparison of the model XSF with experimental results was done for the data obtained from transmission measurement (Fig. 5b) for the sample subjected to external stress of 409.6 MPa and partly unloaded to 50 MPa. In this case, as shown in Eq. (7), the interplanar spacings $< d(\varphi,\psi) >^{\sigma}_{hkl}$ correspond to the loaded sample, while $< d(\varphi,\psi) >^{0}_{hkl}$ are measured after incomplete unloading, and the change of the load was $\sigma^I_{11} = 359.6$ MPa. In this case, the XSFs, determined for the sample's

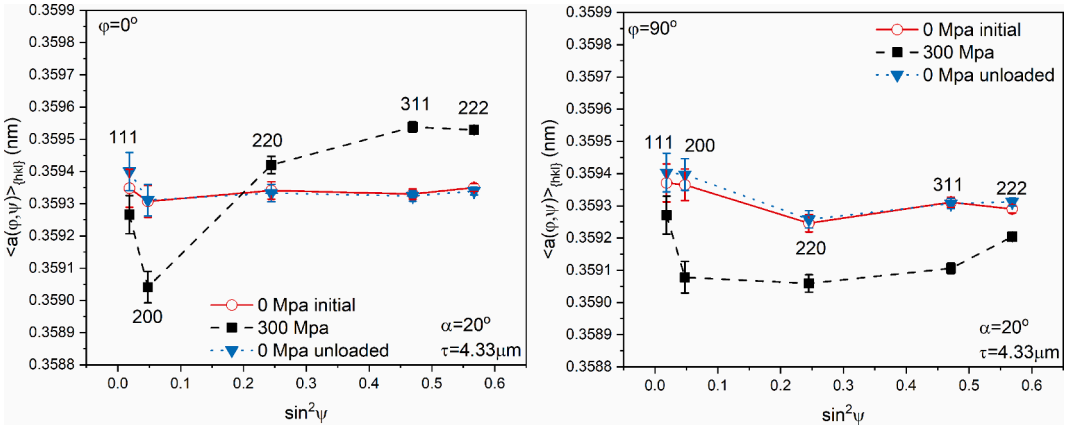

Fig. 6. The example of $\langle a(\varphi,\psi)\rangle_{\{hkl\}}$ vs $sin^2\psi$ plots obtained using MGIXD method during tensile test for the initial, loaded ($\sigma^I_{11} = 300$ MPa) and completely unloaded sample. Error bars correspond to $\delta\{2\theta_{hkl}\} = 0.01°$. For the color figures please refer to the online version of the manuscript.

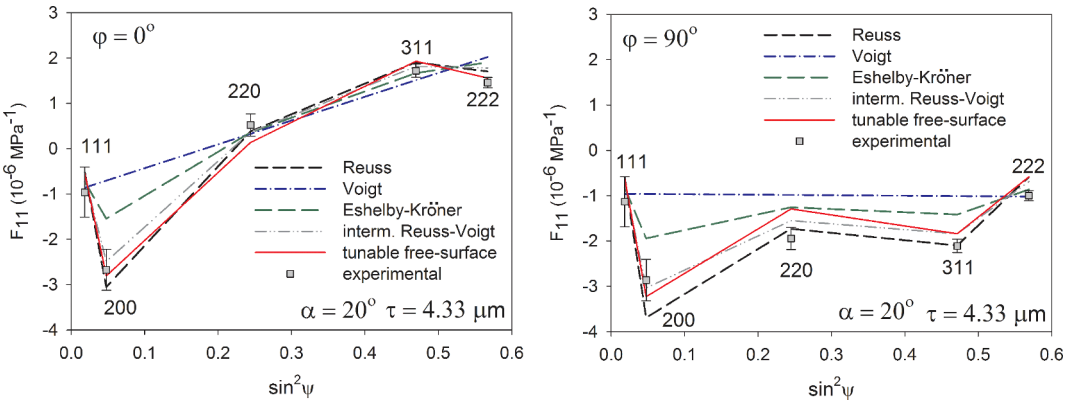

Fig. 7. The F_{11}^{exp} stress factor vs $sin^2\psi$ for φ = 0° and φ = 90° (ψ and φ defined in Fig. 1a) determined using MGIXD method (α = 20°, τ = 4.33 μm) for the sample subjected to the load of 300 MPa and compared to the initial sample. The experimental points are compared with different models (lines). In the tunable free-surface model, calculations were done for optimal parameter $r = 0.74$. For the color figures please refer to the online version of the manuscript.

Table 5
Figure merit values obtained for verified models (in the case of tunable free-surface and intermediate Reuss-Voigt the optimal figures of merit and corresponding *r* or *w* parameters are given).

Verification parameter / Method	Inform. depth (μm)	Voigt	Eshelby-Kroner	Reuss	Tunable free-surface (optimal)	Intermidate Reuss-Voigt (optimal)
δ^2 / MGIXD	*4.33*	*9.82*	*3.27*	*1.58*	*1.07, r = 0.74*	*0.75, w = 0.76*
δ^2 / transmission	∞	*37.17*	*7.84*	*90.53*	*7.84, r = 0*	*8.11, w = 0.37*
χ^2 /MGIXD	*1.9*	*84.63*	*23.62*	*1.77*	*3.36, r = 1*	*1.77, w = 1*
	3.46	*33.10*	*5.82*	*3.24*	*1.12, r = 0.67*	*1.99, w = 0.71*
	4.72	*40.36*	*10.45*	*9.62*	*6.75, r = 0.61*	*7.75, w = 0.65*
χ^2 /MMXD	*4*	*141.4*	*73.9*	*73.8*	*64.62, r = 0,81*	*69.3, w = 0.61*
	10	*86.14*	*63.33*	*70.97*	*61.78, r = 0,36*	*62.96, w = 0.44*
Σ_Δ^2 / MMXD (for 111, 200, 220, 311 reflections)	*4.3 – 26.7*	*947.4*	*470.6*	*551.7*	*419.4, r = 0.27*	*414.3, w = 0.56*

interior, perfectly agree with the Eshelby-Kröner model (see Fig. 8), and this agreement was confirmed by the minimum value of the δ^2 parameter (Eq. (8)) obtained for the intermediate Reuss-Voigt model at $w = 0.37$ (this approach is close to the Kröner model, in the case of a non-textured sample). The Eshelby- Kröner interaction was also confirmed by an *r* value equal to 0 obtained from the tuning of the free-surface model. The optimization results are shown in Fig. S4 (Supplementary Data) and comprised in Table 5.

4.1.2. *Xsfs verification based on quality of lattice strains fitting*

The results of the $\langle a(\varphi,\psi)\rangle_{\{hkl\}}$ vs $sin^2\psi$ plots measured for the mechanically polished sample surface using the AD - MGIXD method with Co radiation are presented in Fig. 9 (the measurements were done for $\varphi = 0°$ and 90°) In these plots, the piecewise linear curve connects the results obtained from least-squares fitting (Eq. (2)) to experimental $\langle a(\varphi,\psi)\rangle_{\{hkl\}}$ vs $sin^2\psi$ dependence. Two independent components of biaxial stress state (σ_{11}^I, σ_{22}^I) and the strain-free lattice parameter a_0 were adjusted in order to minimize the merit function given by Eq. (3). Analysis for different grain interaction models and for three different incident angles (α) corresponding to three different information depths (given in Table 2) was performed. In the case of the intermediate Reuss-Voigt model and the tunable free-surface model, the values of *w* and *r* were optimized and the results are presented in Table 5, together with corresponding figure of merit χ^2 defined in Eq. (3) (the results of optimization are shown in Fig. S5 in Supplementary Data).

It should be noticed that the presented plots are strongly nonlinear and such nonlinearities are caused by significant anisotropy of the single crystal elastic constant of austenite. The largest difference between strains in the 111 and 200 directions is well seen. In contrast to the results presented in Fig. 9, the corresponding plots obtained previously for the W sample are almost perfectly linear, as shown in our previous work [49]. This is certainly the effect of the isotropic elastic properties of W crystallites.

The presented in Fig. 9 results show that the theoretical curves do not agree with the experimental values when the Voigt model calculates XSF. Eshelby-Kröner model also does not fully reflect the experimental results. On the other hand, the XSF values predicted by the Reuss and the tunable free-surface as well as the intermediate Reuss-Voigt models lead to good agreement between fitted lines and experimental points (magnitude of error bar allows such conclusion). The above conclusions are confirmed by the χ^2 presented in Table 5. The prediction of elastic anisotropy obtained with tunable Free-surface model shows that the effect of the free surface is correctly taken into account in calculations of XSFs (cf. Eq. (6)). This effect increases with decreasing depth, i.e. $r \to 1$ for information depths.

The same data analysis as in the case of MGIXD was applied to the experimental results obtained using the ED technique with synchrotron radiation for $\varphi = 0°$ and 90°. The biaxial stress state was assumed for mechanically polished sample and two independent components (σ_{11}^I, σ_{22}^I) as well as the strain-free lattice parameter a_0 were adjusted in the least-squares procedure. The example of $\langle a(\varphi,\psi)\rangle_{\{hkl\}}$ vs $\sin^2\psi$ plots measured with the 111 and 200 reflections, and $2\theta = 16°$, are shown in Fig. 10, together with the lines fitted independently using different models of XSFs.

It should be noticed that for both reflections linear plots were obtained in the case of Reuss, Eshelby-Kröner (with spheroidal inclusion) and Voigt models for which the *hhh* and *h00* reflection do not exhibit nonlinearities for textured sample, as was shown in [19,70]. The perfectly straight lines fitted to experimental results must overlap, however the values of stresses calculated by fitting procedure are different for these models if the single crystal elastic constants are anisotropic. In the case of tunable free-surface model, the $sin^2\psi$ plots are

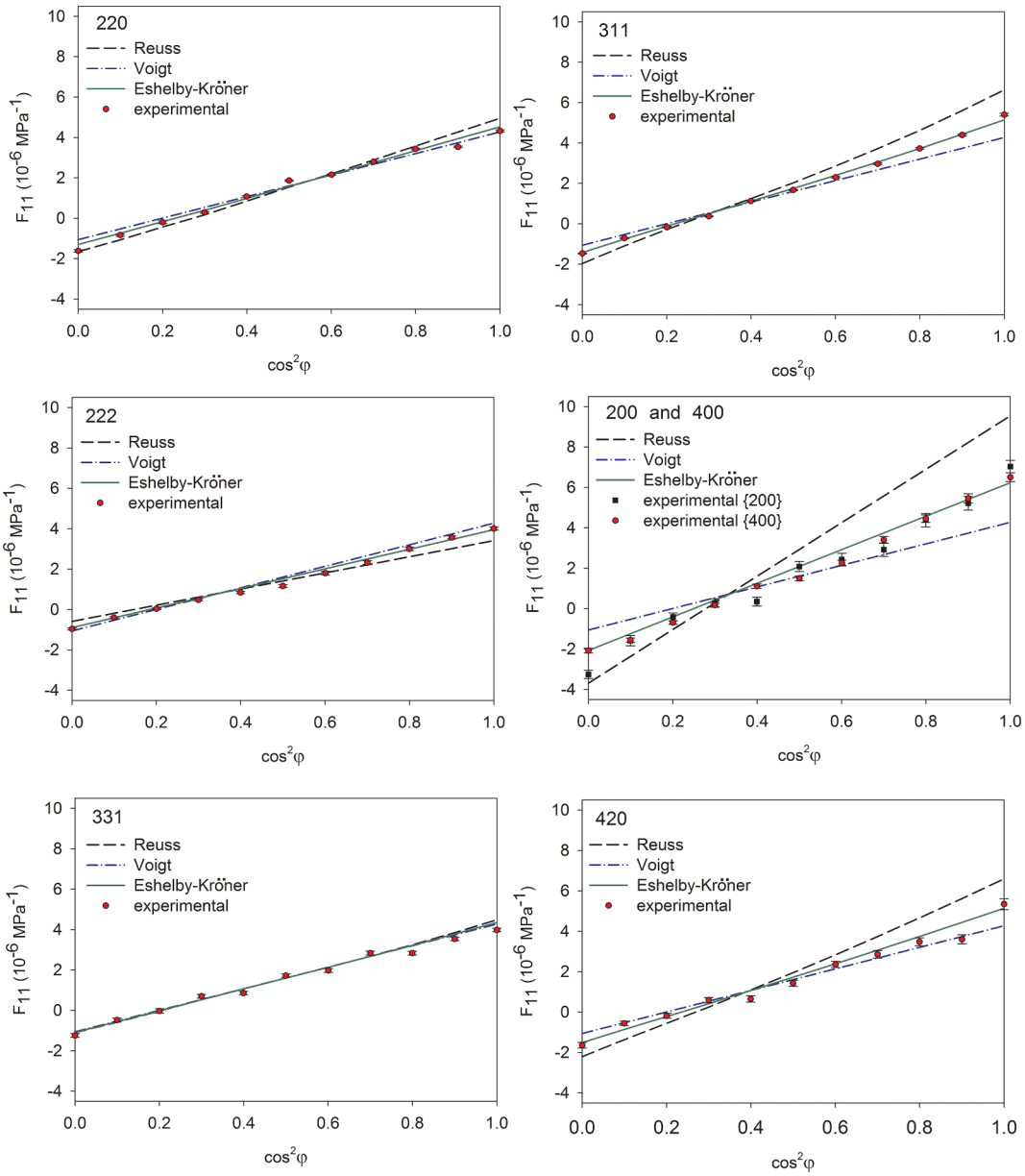

Fig. 8. The F_{11}^{exp} stress factor vs $cos^2\varphi$ for$\psi = 78.3°$ (ψ and φ defined in Fig. 5b) determined using transmission method for the sample subjected to the load corresponding to macroscopic stress of 409.6 MPa and unloaded to 50 MPa. The experimental points are compared with different models (lines). For the color figures please refer to the online version of the manuscript.

generally not linear because the interaction between grains depend on the orientation with respect to the sample [16].

The advantage of the MMPW method (cf. Table 1), in which different average information depths are assigned to $\langle a(\phi,\psi)\rangle_{\{hkl\}}$ vs $\sin^2\psi$ measured for different reflections *hkl,* is its simplicity; however, the information depth for which the stress is determined is wide. Moreover, when the stress is calculated from a single *hkl* reflection, the choice of the proper model for XSFs is not obvious, compared to the case of multiple reflection methods, when $\langle a(\varphi,\psi)\rangle_{\{hkl\}}$ values for many *hkl* reflections are fitted simultaneously to obtain one stress value in a predefined depth, cf. [47,60,67,71]. In the multiple reflection methods, the accordance of the fitted and experimental values $\langle a(\varphi,\psi)\rangle_{\{hkl\}}$ directly verifies if the elastic anisotropy is correctly taken into account in the grain interaction model used for XSF calculation. However, for single reflection (as in the case of MMWP method) the tunable or intermediate models cannot be adjusted to experimental data, because the relations between lattice strains in different crystallographic directions are unknown.

The verification of XSFs on the basis of performed ED measurements can be done using the MMXD method. To do this, it is necessary to select a group of $\langle a(\varphi,\psi)\rangle_{\{hkl\}}$ values measured using different reflections *hkl* sensitive to elastic crystal anisotropy, covering wide range of $\sin^2\psi$ and corresponding to small deviations from the average penetration depth. In the performed experiment, this condition is fulfilled in the case of 111 and 200 reflections for which a wide range of $sin^2\psi$ (equal to 0.8) corresponds to depth $\tau = 4 \pm 2$ μm. This allows us to verify the XSF-model for thin layer close to the surface.

The results of fitting theoretical lines to the selected experimental data obtained using different XSF-models, including the tunable Free-surface and intermediate Reuss-Voigt models are shown in Fig. 11. The verification and optimization of the XSFs was also performed for the depth $\tau = 10 \pm 4$ μm, for which the interplanar spacings were measured using reflections 200, 220 and 311. Results of the verification and optimization of XSF models carried out by minimizing the parameter χ^2

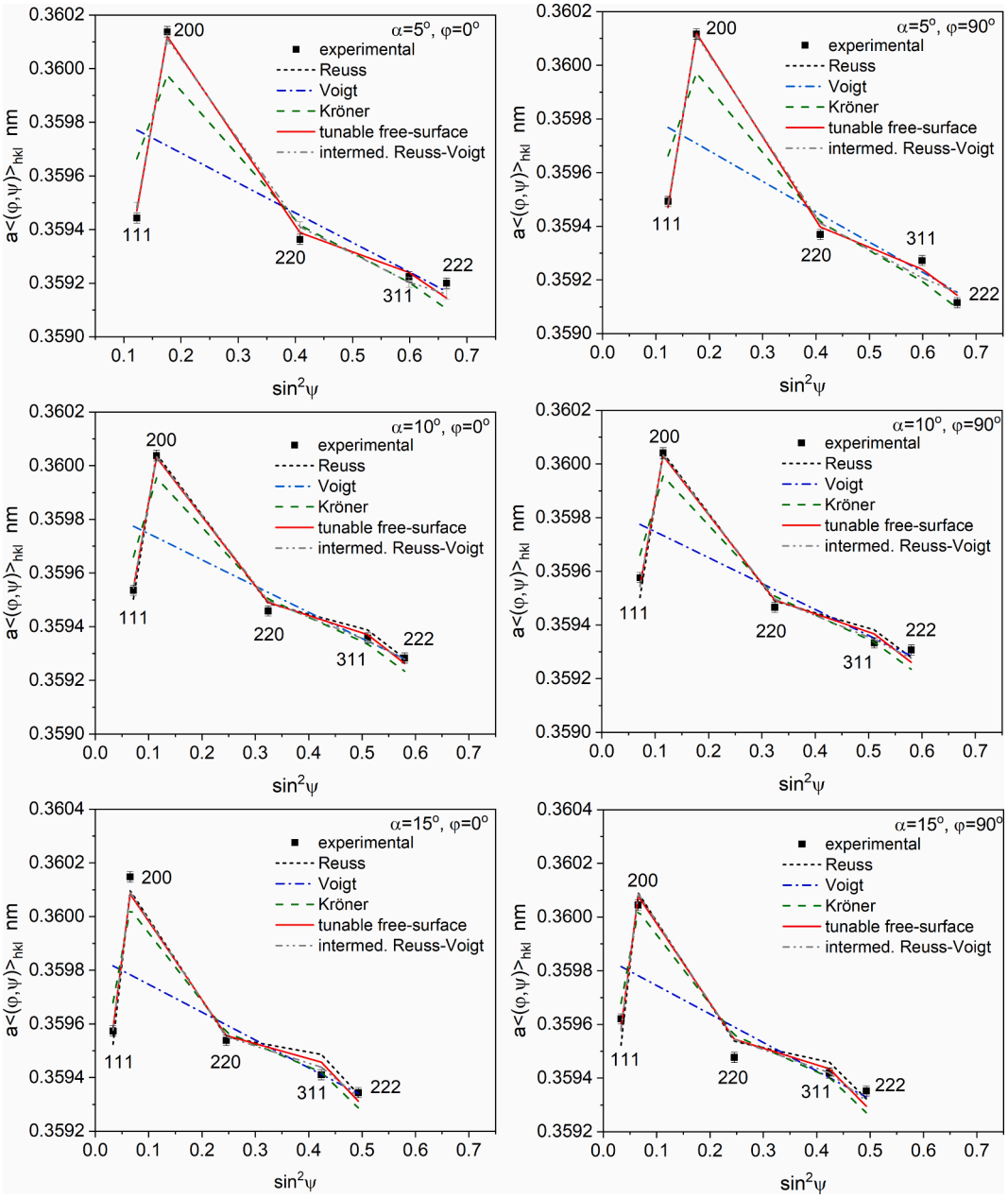

Fig. 9. The example of $\langle a(\varphi,\psi)\rangle_{\{hkl\}}$ vs $sin^2\psi$ plots obtained using MGIXD method for 3 different depths in the polished sample and 5 different grain interaction models. Error bars correspond to $\delta\{2\theta_{hkl}\} = 0.01°$. The plots for Reuss, tunable free-surface, and intermediate Reuss-Voigt model overlap for most cases. For the color figures, please refer to the online version of the manuscript.

are shown in Fig. S6 (Supplementary Data) and comprised in Table 5. It should be emphasized that in the case of MMWP methods the described above optimization cannot be performed for greater depths where the lattice strains are determined using reflections *hkl* which are less sensitive to crystal anisotropy. Indeed, already in the case of optimization performed for $\tau = 10 \pm 4$ μm the minimum of χ^2 is not pronounced (Fig. S6), and almost constant value of χ^2 were obtained when different models were applied for analysis of XSFs in greater depths.

Analyzing the quality of fitting for different XSF models (Table 5 and Fig. S6), it is found, as in the case of the MGIXD method, that the Voigt model cannot be considered in this case because it does not reflect the difference in elastic behavior of grains selected by different *hkl* reflections. The Eshelby-Kröner model fits better to the experimental data, and the best fitting is obtained in the case of the tunable Free-surface and intermediate Reuss-Voigt model (cf. χ^2 in Table 5 and in Fig, S4).. It can be concluded that the use of different *hkl* reflections in the MMXD method allows us to choose the best model for the calculation of XSFs for anisotropic materials at relatively small depth and the results confirm the evolution of *w* and *r* parameters obtained with MGIXD method (i.e. *w* and *r* increase with decreasing depth).

4.1.3. *XSF verification based on stress profile smoothness*

Finally, the criterion given by Eq. (9) was used to find the values of *w* and *r* for which the smoothest function describes the in-depth stress profile obtained using the MMWP method. The optimization can be used for verification of XSF-model within the analyzed range of information depth which is determined by four *hkl* reflection (111, 200, 220, 311). It was found that for deeper depths (and a larger number of *hkl* reflections used in analysis), the optimal values of the *w* and *r* parameters do not change due to the low value of the measured residual stresses and a low sensitivity of the available *hkl* reflections to the crystal anisotropy. This

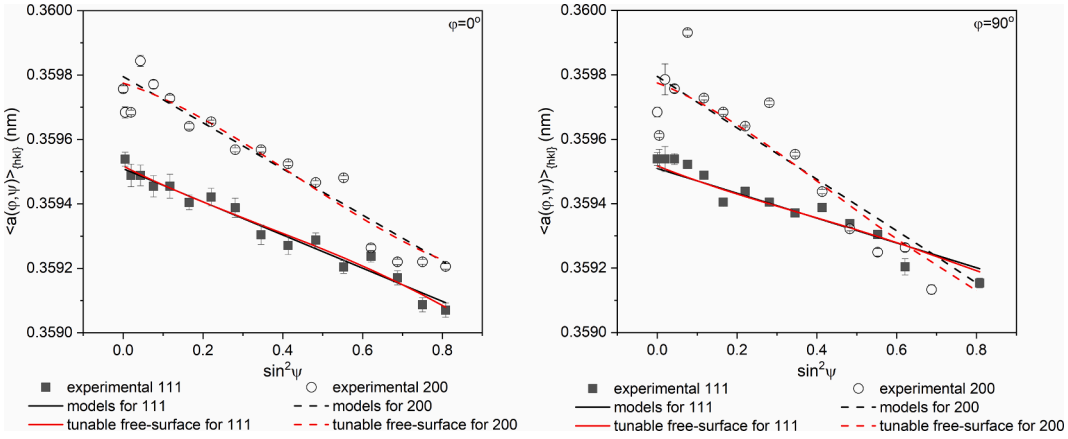

Fig. 10. The example of $\langle a(\varphi,\psi)\rangle_{\{hkl\}}$ vs $sin^2\psi$ plots obtained using ED ($2\theta = 16°$) synchrotron measurements for 111 and 200 reflections analyzed using ED-MMWP method. The lines are fitted to experimental data independently for each reflection *hkl*. In the case of Reuss, Voigt, Kröner and free-surface models the straight lines overlap (small nonlinearity of the plot obtained using free-surface model is seen). For the color figures please refer to the online version of the manuscript.

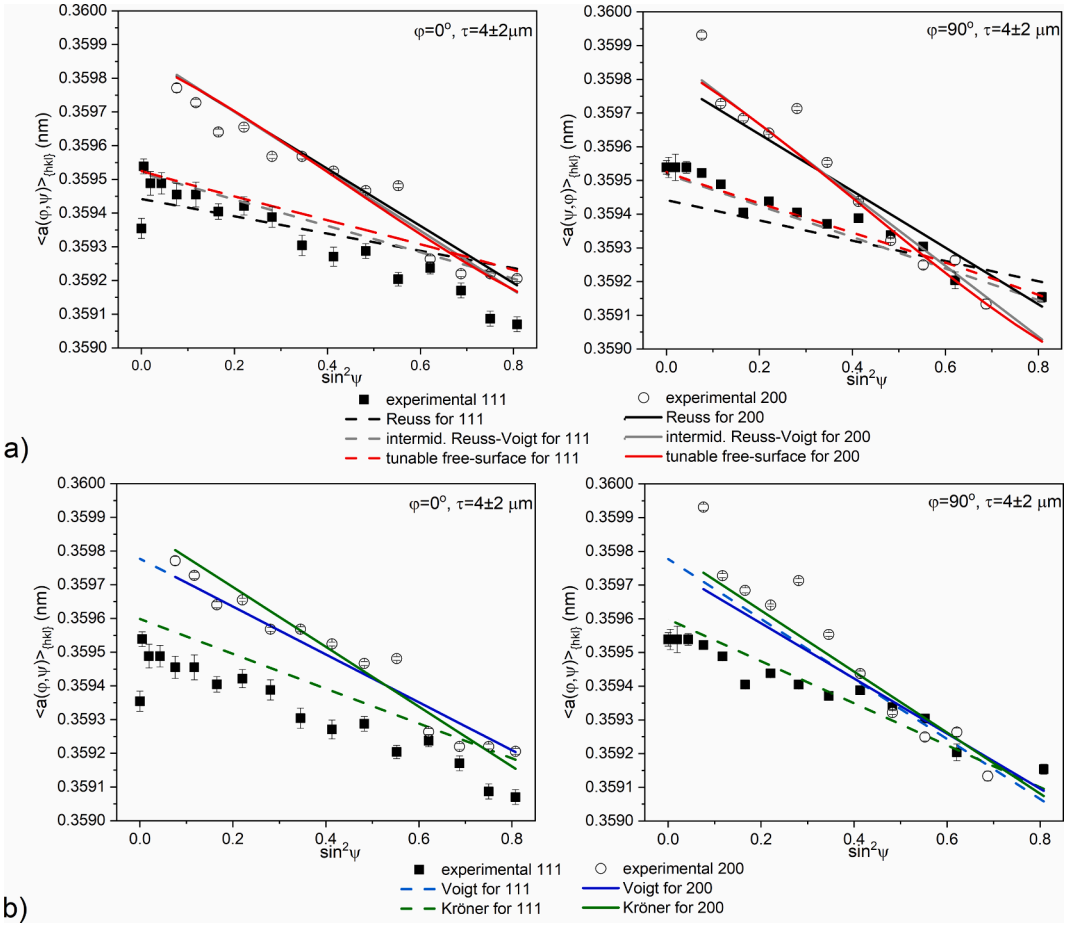

Fig. 11. The example of $\langle a(\varphi,\psi)\rangle_{\{hkl\}}$ vs $sin^2\psi$ plots obtained using ED ($2\theta = 16°$) synchrotron measurements and MMXD method of analysis, presented for information depth $\tau = 4 \pm 2$ μm. The lines are fitted to experimental data for two reflections 111 and 200 simultaneously, using XSFs calculated with a) Reuss and tunable free-surface, as well as b) Voigt and Kröner models. For the color figures please refer to the online version of the manuscript.

means that for depths larger than ca. $\tau \approx 30$ μm we are not able to verify the model of grains interaction. Fortunately, the measurements in the transmission mode showed that for very deep regions ($\tau \to \infty$), the model is very close to Eshelby-Kröner approach (section 4.1.1). The results of optimization based on Σ^2_Δ figure of merit are given in Table 5 and Fig. S7 (Supplementary Data).

4.1.4. *In-depth profile of XSF*

On the basis of the results gathered in Table 5, the dependences of the optimized *w* and *r* parameters are plotted versus information depth in Fig. 12. As presented in this figure, the evolution of the optimal XSF values occurs between Eshelby-Kröner (in bulk material) and Reuss (Fig. 12a) or Free-surface (Fig. 12b) models when approaching sample surface. This means that a significant impact of the surface on the XSFs

was found. It should be emphasized that in the case of tunable Free-surface model the observed effect is well explained by a physical phenomenon, i.e., by the relaxation of the intergranular stresses (or grains interactions) in the direction perpendicular to the surface (cf. Eq. 6).

In this work, for the first time, a method based on inverse Laplace transformation is used to determine the dependence of the r relaxation parameter (tunable free surface model, cf. Fig. 12b) as a function of the real depth z. In this case, the shape of the $r(z)$ function is unknown, however the rapid decrease of the r vs information depth τ suggests also a quick decrease in $r(z)$ dependence. Therefore, it is reasonable to assume the exponential evolution for the $r(z)$ function in the first step of the proposed approach (version 1):.

$$r(z) = a \cdot \exp(-bz), \tag{16}$$

for which $r(\tau)$ the profile can be calculated using the inverse Laplace transformation method:.

$$r(\tau) = a \cdot (b\tau + 1)^{-1}. \tag{17}$$

The function given by Eq. (17) was fitted to the experimental data (cf. Fig. 12b and Table 6).

It was found that so obtained $r(z)$ (Fig. 13 – ver. 1) and $r(\tau)$ (Fig. 12b – ver. 1) functions cannot correctly describe the evolution of r close to the surface because they exceed the maximum value *1* (i.e. $r = 1$ in the tunable free-surface model, meaning a complete relaxation of forces normal to the surface, while $r > 1$ has no physical meaning). Therefore, another theoretical function and its Laplace transform are proposed in order to avoid this problem (version 2):

$$r(z) = 1(z) - 1(z - z_0) + 1(z - z_0)\exp[-b(z - z_0)], \tag{18}$$

$$r(\tau) = a \cdot [1 - \exp(-z_0/\tau)] + a \cdot (b\tau + 1)^{-1}\exp(-z_0/\tau), \tag{19}$$

where $1(z)$ is a Heaviside function and z_0 is the depth for which $r(z < z_0) = 1$.

In such an approach, the complete relaxation of the intergranular stress in the direction perpendicular to the sample was assumed in the subsurface region, i.e. $r(z < z_0) = 1$, which was approximated by $1(z) - 1(z - z_0)$, and the exponential decrease of r was by the value z_0, assuming the constraint $a = 1$ in Eqs. (18) and (19). This assumption is necessary to explain the experimentally determined value $r = 1$ for the information depth of about $\tau = 2$ μm.

The function given by Eq. (19) was fitted to experimental data as shown in Fig. 12b – ver. 2, assuming $z_0 = 3$ μm for which a satisfying agreement between the theoretical line (cf. solid line - ver. 2) and experimental points was obtained. The value of parameter b is given in Table 6, while the $r(z)$ and $r(\tau)$ profiles are presented in Figs. 13 and 12b, respectively. It can be concluded that the solution presented in Fig. 13 (line ver. 2) approximately describes the evolution of the $r(z)$ relaxation factor, i.e. in the subsurface region, the intergranular stresses completely relax in the direction perpendicular to the surface (probably due to the topography of the surface) and the XSFs can be calculated by the free-surface model. It was found that in the studied austenitic sample the relaxation of the intergranular stress in the direction normal to the surface, decreases with increasing real depth z. The faster evolution of

Table 6
Values of adjusted parameters obtained for in-depth profiles vs information depth τ.

	a	b (μm^{-1})	c	d
$\sigma(\tau)$ – stress fitting (Eq. (22))	−579 (MPa)	0.104	44.56 (Pa/μm)	–
$w(\tau)$ – Reuss-Voigt (Eq. (20))	10	7.74	–	0.387
$r(\tau)$ – ver.1 – free-surface (Eq. (17))	1.857	0.411	–	–
$r(\tau)$ – ver.2 – free-surface (Eq.19)	1 (constraint)	0.427	–	–

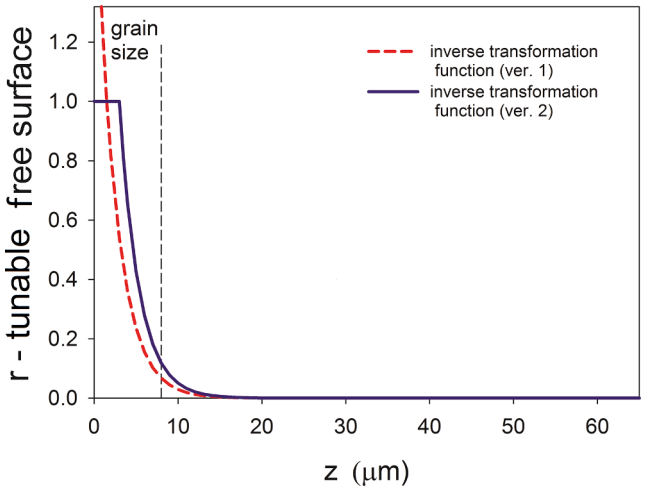

Fig. 13. The in-depth dependence of grain interaction, described by the r parameter in function of the real depth z, for tunable free-surface model. Two approximations of the r evolution are presented for assumptions: Eq. (16) – ver. 1 and Eq. (18) - ver. 2. The dashed line marks the mean grain size of 8 μm.

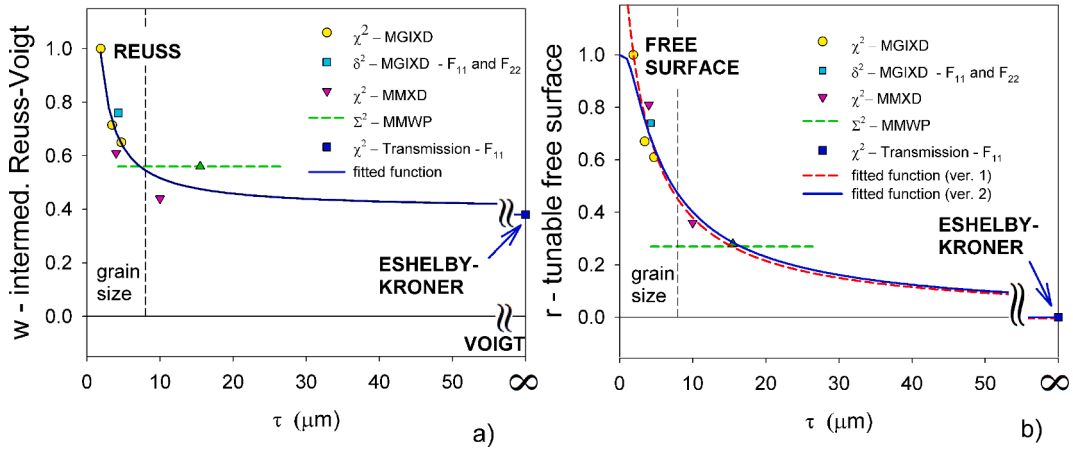

Fig. 12. The in-depth dependence of grain interaction, described by the w parameter intermediate Reuss-Voigt model (a) and r parameter for tunable free-surface model (b). These parameters were determined for different information depths (τ) using different experimental methods and criteria. The experimental results are fitted using functions given by: a) Eq. (20), b) Eq. (17) – ver. 1 and Eq. (19) – ver. 2. For the color figures please refer to the online version of the manuscript.

the r parameter occurs up to a depth approximately equalto the average grain size, while at a depth larger than grain size, the value r approaches zero (Fig. 12b). This means that about one layer of grains is enough to compensate for the Free-surface effect, and the Kröner-Eshelby (bulk material) model can properly describe the interactions between grains. Similar conclusions can be drawn when mean Reuss-Voigt is considered (see Fig. 12a). In this case the experimental data were fitted by the function:

$$w(\tau) = a\cdot(b\tau + 1)^{-1} + d, \tag{20}$$

where the d parameter was added because the $w(\tau)$ approaches the positive value of 0.37 when the model is the Kröner-Eshelby approach.

It was found that in the case of the intermediate Reuss-Voigt model, the fitted $w(\tau)$ line does not match the experimental points (Fig. 12a and Table 6), and the inverse Laplace transform method would give an unambiguous result, therefore the $w(z)$ function was not determined.

4.2. Analysis of stress profile in the polished sample

4.2.1. Stress analysis

As mentioned above, the stress analysis was performed for the mechanically polished austenitic sample assuming biaxial plane stress state, i.e., values of $\sigma^I_{11}, \sigma^I_{22}$, a_0 were adjusted in the least-squares procedure. In the case of the MGIXD method the stress analysis was performed for three depths comprised in Table 2, using the tunable Free surface model with parameter r, which optimal values are given in Table 5. This analysis was already done when the XSF-model was verified in section 4.1.2 and the $\langle a(\varphi,\psi)\rangle_{\{hkl\}}$ vs $sin^2\psi$ are presented in Fig. 9.

As mentioned above the XSF-models cannot be optimized for the ED data obtained using MMWP method, therefore the dependence of the parameter r vs information depth τ (taking into account the in-depth evolution of the model) was used to calculate the F_{ij} factors for different information depths (Fig. 12). So calculated XSFs (tunable Free-surface model) were used to evaluate the stress values from the strains measured at corresponding depths. Example of the model lines fitted independently to experimental points (111 and 200 reflections) are shown in Fig. 10.

To determine the stresses using MMXD method the information depths were selected to ensure the widest possible range of $sin^2\psi$ (Table 2). The values of optimal parameter r used in the tunable Free-surface model for given depths were taken from the fitted line presented in Fig. 12. The model plots $\langle a(\varphi,\psi)\rangle_{\{hkl\}}$ vs $sin^2\psi$ were fitted to experimental values and shown in Fig. 14.

The results presented in Figs. 11 and 14 prove the significant anisotropy of the crystallites in the austenitic sample, which results in relative differences in the slopes of the plot $\langle a(\varphi,\psi)\rangle_{\{hkl\}}$ vs $\sin^2\psi$ corresponding to different hkl reflections and the same information depth. These results should be compared to the corresponding ones obtained for the isotropic W sample, which are presented in our previous paper [49]. In the case of tungsten, regardless the type of used hkl reflection, the pieces of the plot $\langle a(\varphi,\psi)\rangle_{\{hkl\}}$ vs $\sin^2\psi$ compose a linear plot determined for a selected deformation depth.

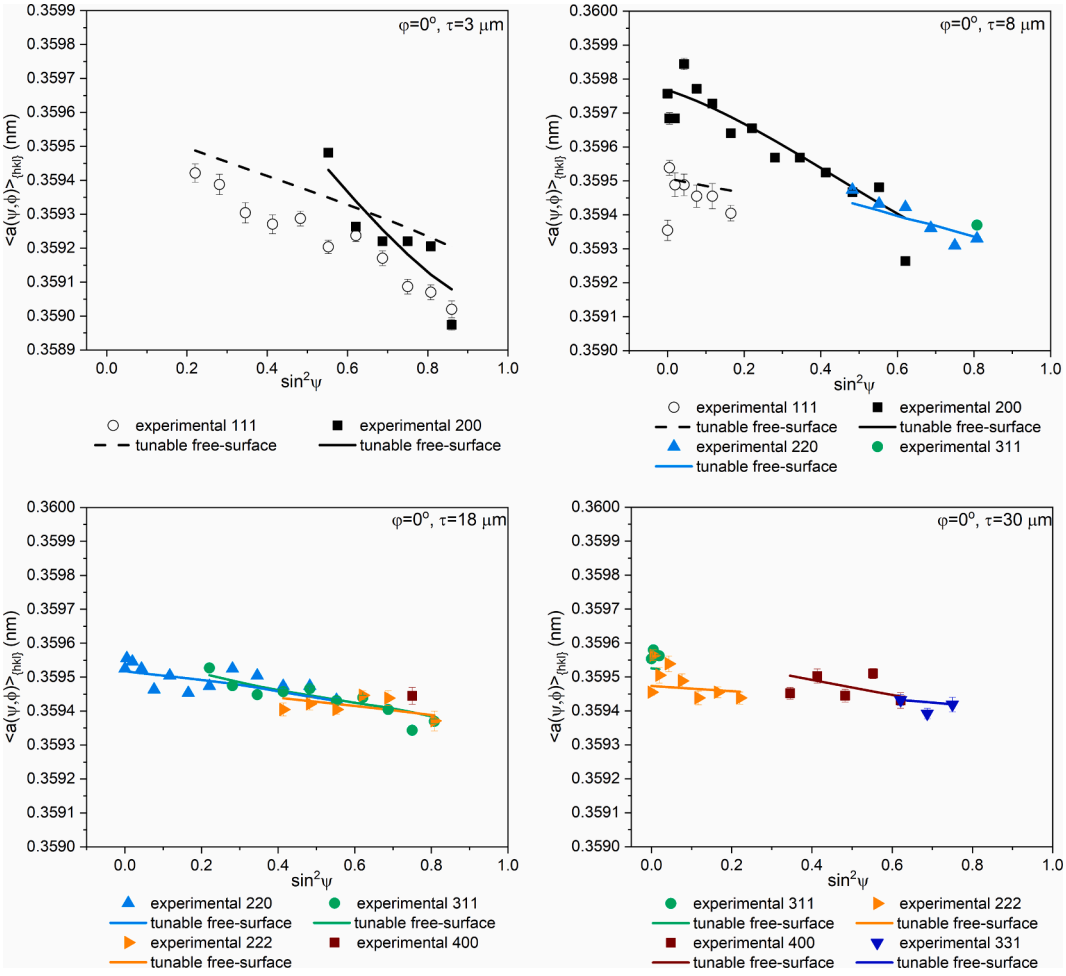

Fig. 14. The example of $\langle a(\varphi,\psi)\rangle_{\{hkl\}}$ vs $sin^2\psi$ plots obtained using ED ($2\theta = 16°$) synchrotron measurements and MMXD method of analysis, presented for four different information depths τ. The tunable free-surface model was used to calculate XSFs. For the color figures please refer to the online version of the manuscript.

It should be emphasized that a significant scatter of the experimental data was observed in the case of the measurements performed with synchrotron radiation (Figs. 11 and 14). This is due to the relatively small number of grains within the information volume (the estimated number is from about 2000 up to dozen thousands) for the configuration with a narrow double-slit system (0.03 mm), scattering angle $2\theta = 16^\circ$, and studied penetration depth of the radiation (given by τ). In this case, a small surface of the sample is seen during the experiment (to the order of tenths of mm^2, depending on the ψ angle).

Conversely, in the case of the experiment performed on the laboratory diffractometer (MGIXD method), the diffracted beam coming from the much larger illuminated surface (a dozen or tens of mm^2), corresponding to the number of 300–600 thousand grains in the information volume. The latter experiment provides very good grain statistics and better representativity of the measured stresses (Fig. 9) compare to synchrotron measurements (Fig. 10 and14). It should be also stated that the results obtained for a large number of grains reduces the influence of the second order plastic incompatibility stresses on the obtained results.

4.2.2. *Stress profile in the polished sample*

The evolutions of strain-free parameter (a_0) and residual stress components σ^I_{11} and σ^I_{22} vs information depth τ determined for mechanically polished sample are shown in Fig. 15. It was found that the stress components σ^I_{11} and σ^I_{22} are approximately equal to each other, which is expected for the applied nondirectional mechanical polishing. To increase the number of experimental data available for further Laplace analysis, the $\sigma^I_{11} \approx \sigma^I_{22}$ condition is introduced and the data are treated together assuming rotational in-plane symmetry. Analyzing Fig. 15, it can be concluded that the results obtained for the polished austenitic sample showed significant evolution of the compressive stress ($\sigma^I_{11} \approx \sigma^I_{22}$) vs information depth τ and an almost constant value of the a_0 parameter for different depths.

As can be seen in Figs. 13 and 14, the results obtained with all methods are consistent, and the complementarity of the measurements can be noted: (a) the AD – MGIXD method with classical X-rays is restricted to a very shallow depth, which is not available for the ED measurements with high energy X-rays; (b) the ED methods characterize stress and strain-free parameter evolution for much deeper layers; (c) the MMXD analysis of the ED data allows for the measurement of the layers close to the surface, being the bridge between AD – MGIXD and ED measurements.

Moreover, it can be stated that both the MGIXD and MMXD methods in which the information depth τ is established within given ranges (Table 2) are used in the region where a significant stress gradient occurs (τ = 0 – 30 μm), while the MMWP method with less strictly defined depth τ (for $\tau > 30$ μm) gives information about stress closing slowly to zero (cf. Fig. 15). The results of the MMWP method are in good agreement with MGIXD and MMXD measurements even in the strong gradient region ($\tau = 5 - 30$ μm). It should be emphasized that the in-depth profile of residual stress was determined by the MGIXD and MMXD methods for well-defined information depths τ. Therefore, the obtained results characterize the stress and XSFs variation vs information depth τ, which can be converted to the stress profile vs real depth z by using the method based on inverse Laplace transform [12,72]. The so obtained stress evolutions can be compared with the grain size. In the present study, the following approach for $\sigma^I(z)$ function was assumed to describe the stress evolution versus real depth z (after [12,72,73]):

$$\sigma^I(z) = (a + cz)\exp(-bz), \tag{21}$$

and the $\sigma^I(\tau)$ calculated from $\sigma^I(z)$ is given by:

$$\sigma^I(\tau) = a\cdot(b\tau + 1)^{-1} + c\cdot\tau\cdot(b\tau + 1)^{-2}, \tag{22}$$

where a, b, and c are unknown parameters.

To determine stress profile vs real depth, the function given by Eq. (22) was fitted to the experimental results (Fig. 15a), and the parameters a, b, and c were determined (Table 6). The values of parameters are substituted to Eq. (21), and the stress profile vs real depth z is found. Subsequently, the stress ($\sigma^I_{11} \approx \sigma^I_{22}$) evolution vs real depth z was plotted in Fig. 16. The same procedure can be applied to determine the evolution of the strain-free lattice parameter vs z if its variation is observed for the $a_0(\tau)$ function.

As presented in Fig. 16, the stress ($\sigma^I_{11} \approx \sigma^I_{22}$) changes with the z-depth from a compressive value (about −500 MPa) near the surface, through tensile stress (about 40 MPa) for $z \approx 23$ μm, toward 0 MPa in deeper regions for $z > 60$ μm. This stress evolution can be explained by the mechanical equilibrium condition [11]. As it is seen in Fig. 6, small lattice strains (and stresses) were found in the initial sample. Therefore, significant compressive stress introduced due to the mechanical polishing in the subsurface layers should be compensated by the tensile stress in a deeper layer. The latter stress, being a response to this compressive stress leading to the mechanical equilibrium of the material for which the net force acting on the total cross-sectional area of the specimen should be equal to zero [11,74].

5. Discussion

Two non-destructive methods for residual stress determination were applied to study the stress and the strain-free lattice parameter in an elastically anisotropic austenitic stainless steel sample subjected to

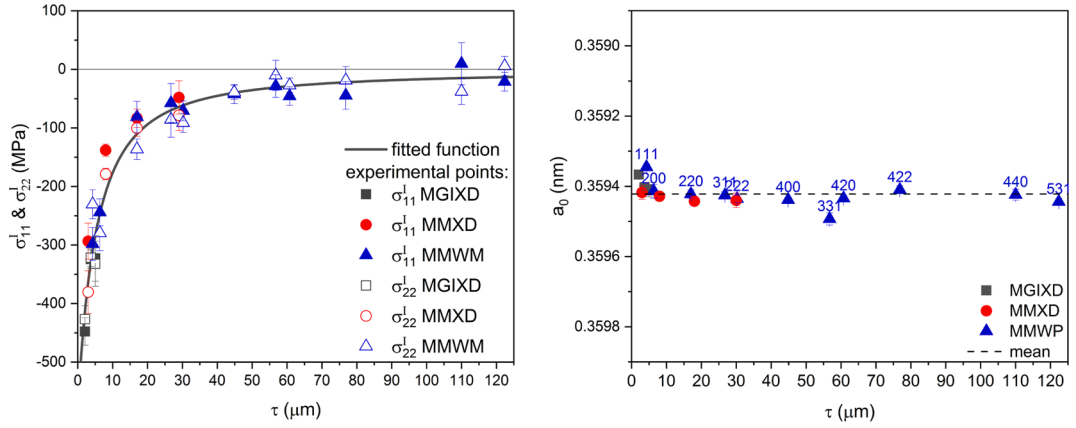

Fig. 15. The profile of residual stresses $\sigma^I_{11} \approx \sigma^I_{22}$ (a) and lattice parameter a_0 (b) as a function of τ – information depth. Results gathered from classical diffractometer (AD – MGIXD method) and synchrotron EDDI experiment (MMXD and MMWM analysis of ED results for $2\theta = 16^\circ$). The tunable free-surface grain interaction model was used in the analysis. The experimental results in a) are fitted using function given by Eq. 23.

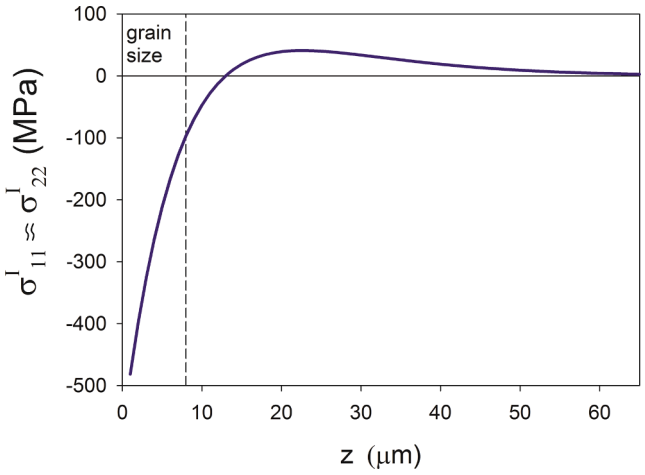

Fig. 16. The in-depth dependence of grain interaction, described by the stresses $\sigma_{11}^{I} \approx \sigma_{22}^{I}$ in function of the real depth z, for tunable free-surface model. The assumed stress evolution function is given by Eq. (22). The dashed line marks the mean grain size of 8 μm.

mechanical polishing. High-energy synchrotron radiation allowed measurements for significantly larger subsurface depths than classical laboratory X-rays. The results of the multi-reflection grazing incidence X-ray diffraction method (AD-MGIXD) and energy dispersive analysis (ED- MMWP or MMXD) were compared, showing their complementary character. An excellent continuation and overlapping of the results was obtained using different data analysis methodologies (i.e., MGIXD, MMWP, and MMXD).

The applied methodologies provide a wide range of depths at which the stress gradient can be determined. A compressive stress of about −500 MPa is found very close to the polished surface (MGIXD method). Going deeper in the subsurface volume, the residual stresses gradually change to tensile stress (necessary for material equilibrium) and then decrease to zero value at a depth of about 60 μm (MMXD and MMWP methods). The strain-free lattice parameter value remains constant (in the margin of ± 0.001 Å), regardless of the method used to determine it.

The results presented in this paper concerning the in-depth evolution of the grain interaction model constitute the first comprehensive attempt to solve this problem. The evolution between free-surface (surface) and Eshelby-Kröner (bulk) was described by the exponential decrease of the $r(z)$ parameter expressing the vanishing of grain interaction (the same stress for all grains as in the Reuss model) in the direction perpendicular to the free surface. This means that the in-plane interaction is of the Eshelby-Kröner type and is constant regardless of the depth below the surface, while the out-of-plane interaction changes from free surface type for $z \to 0$ towards Eshelby-Kröner for greater depth. It was found that the faster evolution of the $r(z)$ parameter occurs up to a depth approximately equal to average grain size, and at this depth approaches zero value. This means that one layer of grains is enough to compensate for the free-surface effect, and the Eshelby-Kröner model can properly describe the interactions between grains in deeper material zones. Similar conclusions can be drawn when mean Reuss-Voigt is considered; however, in this case, the fitted line does not match the experimental points.

The obtained results are not yet general and were verified for one specific case of an austenitic sample subjected to mechanical polishing. Some of the proposed methods are general and can be applied for any single phase polycrystalline sample, as a development of the tunable free-surface method for XSF and the verification test based on '*in-situ*' measurements. In this verification the effects of such phenomena as second order plastic incompatibility stresses or/and stacking faults are excluded. However, particular attention should be paid when the model verification is based on the fitting quality of the interplanar spacings, because of the potential influence of the above mentioned phenomena on the obtained results. The significant values of the second order plastic incompatibility stresses are usually determined on the basis of non-linearities measured on a $sin^2\psi$ plot using single or multiple *hkl* reflections, for example in the samples subjected to monotonic plastic deformation occurring progressively in the same direction as for example rolling [16,75] or uniaxial tensile [76–78], but they are not significant in the case of nondirectional treatments such as mechanical polishing [12,60]. The previously determined impact of the stacking faults on the measured lattice strains is less significant compare to that caused by the elastic anisotropy [59]. It is also worth noting that small nonlinearities were observed in the initial sample as shown in Fig. 6.

In the case of the results presented in this work very good agreement was obtained between verification methods based on relative strains measured during the tensile test (avoiding the problems with impact of initial plastic incompatibility stresses or/and stacking faults) with those in which the measured interplanar spacings are fitted by theoretical functions. Therefore, it can be concluded that influence of unwanted phenomena on the obtained results is not significant compare to the impact of the studied elastic anisotropy and grain interactions. It should be also emphasized that the methods applied in this work can be used exclusively in the case of single phase materials and the problem of grains interactions between phases is more complex as shown in recent works [78–80].

It should be emphasized that the repeatability of the results and the convergence of the results obtained from tunable models using different methods of measurement (ED and AD techniques, cf. Fig. 12) and different methods of verifications (e.g., during tensile test) exclude doubts whether the observed effects are caused by statistical errors or systematic errors such as diffractometer misalignment. Therefore, the obtained results should be related to systematic effects caused by physical reason, in this case the influence of the free surface on the intergranular interactions occurring in polycrystalline material. This effect is taken into account in the tunable Free-surface model. The results presented in this work showed that for the studied sample the relaxation of the intergranular stresses in the direction perpendicular to the surface occurs in one layer of grains having approximately equiaxed grains, and this effect significantly decreases with increasing depth. This information has an important practical significance, i.e. it means the Eshelby-Kröner model is applicable for measurements in which the penetration/information depth is significantly larger than mean grain size, including the measurements performed using standard Ψ or Ω-geometry with characteristic radiation produced by usually used tubes in the energy range 4–18 keV [12] or synchrotron radiation above 4 keV performed for many metal or ceramic samples. The conclusion of this work is that in the that use of the Reuss or free-surface model must be considered in the case when the penetration depth of the used radiation is in order of grain size, especially in the case of Laplace space methods. In this case, it is strongly recommended to verify the XSF-model, at least by checking the quality of data fitting or/and difference between stresses determined using the 111 and 200 reflections, which are the most influenced by elastic anisotropy for fcc crystals.

It should be also mentioned that the significant nonlinearities of the $sin^2\psi$ plots (when multiple reflections *hkl* are measured) can lead to significant errors in stress analysis. It is well known, that to determine the stress from linear regression as wide as possible range of $sin^2\psi$ is recommended [11,12]. Even if the plot is linear in the case of single reflection measurement the range at least 0.5 range is required. As seen in the case of MGIXD method this requirement is difficult to fulfill and the measurement for highly anisotropic reflections such as 111 and 200 must be performed. Therefore, the tuning of the XSF-model should be done and can be done only if the sufficient range of $sin^2\psi$ plot is available as in this work (cf. Figs. 7-9). The choice of the X-ray tube is certainly important to ensure the appropriate information depth and range of available $sin^2\psi$ range. Similar requirements concerns the MMXD method in which the compromise between the available $sin^2\psi$ range (as large as

possible) and corresponding range of information depth (as small as possible) must be reached. This condition can be also modified by setting different values of 2θ angle. The problem of XSFs anisotropy plays an important role for the measurements for smallest possible depth when the 111 and 200 reflections are used. It is recommended to adjust the tunable model for the $sin^2\psi$ plot containing results obtained using both reflections. In this case the appropriate values of XSFs can be found, what is not possible when the analysis is done only for single reflection. In the latter case the XSFs are unknown, leading to significant systematic error (as mentioned in the Introduction the stress value can be 2.4 times larger for if the analysis is done for reflection 200, using the Voigt model compared to the Reuss).

Further development of the work concerning in-depth variation of grain interaction and verification of XSF is in progress. Especially important is the correlation of this evolution with the grain size and the shape of the grains. Open question is how general is the conclusion that the most significant evolution of XEC, caused by free surface, occurs at the subsurface layer having a thickness of about the mean size of grains. Another question is how the microstructure influences the relaxation of the intergranular stresses in the direction perpendicular to the sample, especially in the context of the works showing that the Vook-Witt model gives the best results for columnar microstructure [14,28], while the Reuss or free-surface models are the best in the case of flat grains after a cold rolling process [16,22]. Moreover, many examples of significant deviations from the Eshelby-Kröner model for other materials have been shown in handbooks [12]. To answer these questions, measurements using the most objective method with the relative lattice strains determined during '*in-situ*' tensile testing will be done for different materials exhibiting different sizes and shapes of the grains. To do this, the monochromatic characteristic X-ray radiation (MGIXD method) as well as braking radiation (MMXD) will be applied. Bremsstrahlung can be used due to an important breakthrough achieved recently in development of laboratory diffraction by the application of Metal Jet X-ray tubes, in which the anode consists of liquid metals (e.g. 80 % of gallium and 20 % of indium) [81,82]. Due to the wide energy spectrum (up to 72 keV used in [82]) and very high intensity of the produced X-rays this equipment is nowadays suitable for many methods which were previously used only with synchrotron radiation, including the Laplace space methods [82]. It is worth noting, that there are alternative ways of development methodologies presented in this work. From the experimental point of view instead of use high energy radiation the MGIXD method can be combined with the layer removal method in order to reach resolution of 1–2 μm in depth analysis (in similar way as in [9]). In this case, measurements can be made for any depth, but it should be emphasized that the stress state changes as a result of layer removing. Regarding the theoretical models for the calculation of XSF, the effect of free surface on intergranular interactions can also be investigated by combining the crystallographic model with finite element calculations. This way of theoretical study is considered to be a further development.

6. Summary

On the basis of the presented results the following conclusions can be drawn:

1. Using the complementary Laplace space methods with Co K_α radiation (MGIXD) and high energy synchrotron radiation (MMWP and MMXD), the evolution of the stress in mechanically polished austenitic sample was determined up to the depth of about 60 μm. A significant compressive stress of about −500 MPa was found close to the surface, which changes to tensile stress (necessary for material equilibrium) in the deeper zone of the sample.

2. Significant in-depth variation of intergranular interaction was found close to the sample surface. This effect can be explained by the tunable free-surface model, taking into account the relaxation of the intergranular stress components being perpendicular to the surface.

3. The important practical message of this work for researchers using neutron and X-ray diffraction methods for stress analysis is that the proper model of XSF must be used to ensure the trueness of the obtained results. As shown in the present work, in austenitic sample with equiaxed grains the commonly used Eshelby-Kröner is applicable when the information depth significantly exceeds the subsurface layer having a thickness of about mean grain size. When the measurements are performed for smaller depths, the Reuss, free-surface or tunable models should be used.

4. It is still an open question what the impact of grain size and microstructure on the grain interaction model is, especially in the case of the subsurface zone of the sample. This problem requires further study, which should be done for different materials.

CRediT authorship contribution statement

M. Marciszko-Wiąckowska: Conceptualization, Methodology, Software, Validation, Formal analysis, Investigation, Writing – review & editing, Project administration. **A. Oponowicz:** Data curation, Formal analysis, Investigation, Writing – original draft. **A. Baczmański:** Conceptualization, Methodology, Writing – review & editing, Funding acquisition. **Ch. Braham:** Formal analysis. **M. Wątroba:** Formal analysis, Investigation. **M. Wróbel:** Writing – review & editing. **M. Klaus:** Conceptualization, Investigation, Methodology. **Ch. Genzel:** Conceptualization, Investigation, Methodology, Writing – review & editing.

Declaration of Competing Interest

The authors declare that they have no known competing financial interests or personal relationships that could have appeared to influence the work reported in this paper.

Acknowledgments

This work was financed by grant from the National Science Centre, Poland (NCN): UMO-2017/25/B/ST8/00134. Research project was partly supported by the program "Excellence initiative – research university" for the AGH University of Science and Technology. A.O. has been partly supported by the EU Project POWR.03.02.00-00-I004/16. Furthermore, we would like to thank Helmholtz-Zentrum Berlin für Materialien und Energie for the beamtime provided at the 7 T-MPW-EDDI beamline (BESSY II, HZB, Berlin, Germany).

Appendix A. Supplementary data

Supplementary data to this article can be found online at https://doi.org/10.1016/j.measurement.2022.111016.

References

[1] M. Hayashi, Residual Stresses Induced by Surface Working and Their Improvement by Emery Paper Polishing, Quantum Beam Sci. 4 (2020) 21, https://doi.org/10.3390/qubs4020021.

[2] N.S. Prabhu, J. Joseyphus, T.S.N. Sankaranarayanan, B.R. Kumar, A. Mitra, A. K. Panda, Residual Stress Analysis in Surface Mechanical Attrition Treated (SMAT) Iron and Steel Component Materials by Magnetic Barkhausen Emission Technique, IEEE Trans. Magn. 48 (12) (2012) 4713–4717, https://doi.org/10.1109/TMAG.2012.2203141.

[3] M. Kattoura, S.R. Mannava, D. Qian, V.K. Vasudevan, Effect of laser shock peening on residual stress, microstructure and fatigue behavior of ATI 718Plus alloy, Int. J. Fatigue C (2017) 121–134, https://doi.org/10.1016/j.ijfatigue.2017.04.016.

[4] P. Vourna, An accurate method for determining residual stresses with magnetic non-destructive techniques in welded ferromagnetic steels, IOP Conf. Ser.: Mater. Sci. Eng. 108 (2016), 012017, https://doi.org/10.1088/1757-899X/108/1/012017.

[5] R. Sun, L. Li, Y. Zhu, W. Guo, P. Peng, B. Cong, J. Sun, Z. Che, B. Li, C. Guo, L. Liu, Microstructure, residual stress and tensile properties control of wire-arc additive manufactured 2319 aluminum alloy with laser shock peening, J. Alloy. Compd. 747 (2018) 255–265, https://doi.org/10.1016/j.jallcom.2018.02.353.

[6] X. Cheng, J.W. Fisher, H.J. Prask, T. Gnäupel-Herold, B.T. Yen, S. Roy, Residual stress modification by post-weld treatment and its beneficial effect on fatigue

strength of welded structures, Int. J. Fatigue 25 (2003) 1259–1269, https://doi.org/10.1016/j.ijfatigue.2003.08.020.
[7] T. Guo, Y. Chen, R. Cao, X. Pang, J. He, L. Qiao, Cleavage cracking of ductile-metal substrates induced by brittle coating fracture, Acta Mater. 152 (2018) 77–85, https://doi.org/10.1016/j.actamat.2018.04.017.
[8] E. Maleki, S. Bagherifard, O. Unal, M. Bandini, G.H. Farrahi, M. Guagliano, Introducing gradient severe shot peening as a novel mechanical surface treatment, Sci Rep. 11 (2021) 22035, https://doi.org/10.1038/s41598-021-01152-2.
[9] A. Fischer, S. Degener, A. Liehr, T. Niendorf, Evaluation of extremely steep residual stress gradients based on a combined approach using laboratory-scale equipment, J Appl Cryst. 54 (2021) 1793–1798, https://doi.org/10.1107/S1600576721010335.
[10] A. Malekahmadi, M. Honarpisheh, Investigation of shot blasting and thermal stress relieving processes on residual stresses and corrosion behavior of X60 steel gas pipelines, SN Appl. Sci. 2 (2020) 1593, https://doi.org/10.1007/s42452-020-03420-8.
[11] I.C. Noyan, J.B. Cohen, Residual stress: measurement by diffraction and interpretation, Springer-Verlag, New York, 1987.
[12] V. Hauk, Structural and Residual Stress Analysis by Nondestructive Methods, Elsevier, 1997. 10.1016/b978-0-444-82476-9.50022-0.
[13] W. Reimers, A.R. Kaysser-Pyzalla, A. Schreyer, H. Clemens, Neutrons and Synchrotron Radiation in Engineering Materials Science From Fundamentals to Material and Component Characterization, 2008. https://nbn-resolving.org/urn:nbn:de:101:1-2014081313663 (accessed December 26, 2021).
[14] U. Welzel, J. Ligot, P. Lamparter, A.C. Vermeulen, E.J. Mittemeijer, Stress analysis of polycrystalline thin films and surface regions by X-ray diffraction, J Appl Cryst. 38 (1) (2005) 1–29, https://doi.org/10.1107/S0021889804029516.
[15] E. Macherauch, H. Wohlfahrt, U. Wolfstieg, Practical sefinition of residual stresses, Harterei Tech. Mitt. 28 (1973) 201–211.
[16] A. Baczmanski, P. Lipinski, A. Tidu, K. Wierzbanowski, B. Pathiraj, Quantitative estimation of incompatibility stresses and elastic energy stored in ferritic steel, J Appl Cryst. 41 (5) (2008) 854–867, https://doi.org/10.1107/S0021889808023911.
[17] W. Voigt, Lehrbuch der Kristallphysik, 1928.
[18] A. Reuss, Berechnung der Fließgrenze von Mischkristallen auf Grund der Plastizitätsbedingung für Einkristalle, Z. angew. Math. Mech. 9 (1) (1929) 49–58, https://doi.org/10.1002/zamm.19290090104.
[19] H. Dölle, J.B. Cohen, Evaluation of (residual) stresses in textured cubic metals, Metall. Trans. A 11 (5) (1980) 831–836, https://doi.org/10.1007/BF02661212.
[20] M. Barral, J. Lebrun, J. Sprauel, G. Maeder, X-ray macrostress determination on textured material; use of the ODF for calculating the X-ray compliances, Metall. Trans. A, Phys. Metall. Mater. Sci. 18 (1987) 1229–1238, https://doi.org/10.1007/BF02647192.
[21] C.M. Brakman, The Voigt model case, Philos. Mag. A 55 (1) (1987) 39–58, https://doi.org/10.1080/01418618708209799.
[22] A. Baczmański, K. Wierzbanowski, W.G. Haije, R.B. Helmholdt, G. Ekambaranathan, B. Pathiraj, Diffraction Elastic Constants for Textured Materials — Different Methods of Calculation, Cryst. Res. Technol. 28 (2) (1993) 229–243, https://doi.org/10.1002/crat.2170280217.
[23] E. Kröner, Berechnung der elastischen Konstanten des Vielkristalls aus den Konstanten des Einkristalls, Z. Physik. 151 (4) (1958) 504–518, https://doi.org/10.1007/BF01337948.
[24] J.D. Eshelby, The determination of the elastic field of an ellipsoidal inclusion, and related problems, Collected Works of J. D. Eshelby. 241 (2007) 209–229, https://doi.org/10.1007/1-4020-4499-2_18.
[25] S. Fréour, J. Fajoui, Eshelby-Kröner self-consistent elastic model: the geometric mean versus the arithmetic mean - A numerical investigation, Z. Angew. Math. Mech. 92 (2012) 329–338, https://doi.org/10.1002/zamm.201100135.
[26] R.W. Vook, F. Witt, Thermally induced strains in evaporated films, J. Appl. Phys. 36 (7) (1965) 2169–2171, https://doi.org/10.1063/1.1714442.
[27] M. van Leeuwen, J.-D. Kamminga, E.J. Mittemeijer, Diffraction stress analysis of thin films: Modeling and experimental evaluation of elastic constants and grain interaction, J. Appl. Phys. 86 (1999) 1904–1914, https://doi.org/10.1063/1.370986.
[28] U. Welzel, E.J. Mittemeijer, Diffraction stress analysis of macroscopically elastically anisotropic specimens: On the concepts of diffraction elastic constants and stress factors, J. Appl. Phys. 93 (2003) 9001–9011, https://doi.org/10.1063/1.1569662.
[29] M.E. Fitzpatrick, A. Lodini, in: Analysis of Residual Stress by Diffraction using Neutron and Synchrotron Radiation, CRC Press, London, 2003, https://doi.org/10.1201/9780203608999.
[30] W. Woo, V.T. Em, B.S. Seong, P. Mikula, G.B. An, Residual stress determination in a thick ferritic steel weld plate using neutron diffraction, J. Mater. Sci. 47 (14) (2012) 5617–5623, https://doi.org/10.1007/s10853-012-6456-5.
[31] T. Tsakalakos, M. Croft, N. Jisrawi, R. Holtz, Z. Zhong, Measurement of Residual Stress Distributions by Energy Dispersive X-ray Diffraction Synchrotron Radiation, Proceedings of the International Offshore and Polar Engineering Conference, 2006.
[32] C. Genzel, I.A. Denks, M. Klaus, Residual Stress Analysis by X-Ray Diffraction Methods, in: Modern Diffraction Methods, John Wiley & Sons, Ltd, 2013, pp. 127–154, https://doi.org/10.1002/9783527649884.ch5.
[33] S.J.B. Kurz, S.R. Meka, N. Schell, W. Ecker, J. Keckes, E.J. Mittemeijer, Residual stress and microstructure depth gradients in nitrided iron-based alloys revealed by dynamical cross-sectional transmission X-ray microdiffraction, Acta Mater. 87 (2015) 100–110, https://doi.org/10.1016/j.actamat.2014.12.048.
[34] M. Drakopoulos, T. Connolley, C. Reinhard, R. Atwood, O. Magdysyuk, N. Vo, M. Hart, L. Connor, B. Humphreys, G. Howell, S. Davies, T. Hill, G. Wilkin, U. Pedersen, A. Foster, N. De Maio, M. Basham, F. Yuan, K. Wanelik, I12: the Joint Engineering, Environment and Processing (JEEP) beamline at Diamond Light Source, J. Synchrotron Rad. 22 (2015) 828–838, https://doi.org/10.1107/S1600577515003513.
[35] C.h. Genzel, I.A. Denks, R. Coelho, D. Thomas, R. Mainz, D. Apel, M. Klaus, Exploiting the features of energy-dispersive synchrotron diffraction for advanced residual stress and texture analysis, J. Strain Anal. Eng. Des. 46 (7) (2011) 615–625, https://doi.org/10.1177/0309324711403824.
[36] M. Meixner, T. Fuss, M. Klaus, C. Genzel, Diffraction analysis of strongly inhomogeneous residual stress depth distributions by modification of the stress scanning method, I. Theoretical concept, J Appl Cryst. 48 (2015) 1451–1461, https://doi.org/10.1107/S160057671501448X.
[37] V. Savaria, F. Bridier, P. Bocher, Computational quantification and correction of the errors induced by layer removal for subsurface residual stress measurements, Int. J. Mech. Sci. 64 (1) (2012) 184–195, https://doi.org/10.1016/j.ijmecsci.2012.07.003.
[38] C.h. Genzel, M. Broda, D. Dantz, W. Reimers, A self-consistent method for X-ray diffraction analysis of multiaxial residual-stress fields in the near-surface region of polycrystalline materials. II. Examples, J. Appl. Crystallogr. 32 (4) (1999) 779–787, https://doi.org/10.1107/S0021889899005518.
[39] C.h. Genzel, C. Stock, W. Reimers, Application of energy-dispersive diffraction to the analysis of multiaxial residual stress fields in the intermediate zone between surface and volume, Mater. Sci. Eng., A 372 (2004) 28–43, https://doi.org/10.1016/j.msea.2003.09.073.
[40] H. Ruppersberg, I. Detemple, J. Krier, Evaluation of strongly non-linear surface-stress fields σxx(z) and σyy(z) from diffraction experiments, Phys. Status Solidi (a). 116 (2) (1989) 681–687.
[41] C.h. Genzel, I.A. Denks, J. Gibmeier, M. Klaus, G. Wagener, The materials science synchrotron beamline EDDI for energy-dispersive diffraction analysis, Nucl. Instrum. Methods Phys. Res., Sect. A 578 (1) (2007) 23–33, https://doi.org/10.1016/j.nima.2007.05.209.
[42] B. Ballard, P. Predecki, T. Watkins, K. Kozaczek, D. Braski, C. Hubbard, Depth Profiling Biaxial Stresses in Sputter Deposited Molybdenum Films; Use of the Cos2ϕ Method, in: 1997: pp. 363–370. 10.1007/978-1-4615-5377-9_40.
[43] A. Kumar, U. Welzel, E.J. Mittemeijer, Depth dependence of elastic grain interaction and mechanical stress: Analysis by x-ray diffraction measurements at fixed penetration/information depths, J. Appl. Phys. 100 (2006), 114904, https://doi.org/10.1063/1.2363899.
[44] T. Erbacher, A. Wanner, T. Beck, O. Vöhringer, X-ray diffraction at constant penetration depth – a viable approach for characterizing steep residual stress gradients, J. Appl. Crystallogr. 41 (2) (2008) 377–385, https://doi.org/10.1107/S0021889807066836.
[45] K. Van Acker, L. De Buyser, J.P. Celis, P. Van Houtte, Characterization of thin nickel electrocoatings by the low-incident-beam-angle diffraction method, J Appl Cryst. 27 (1) (1994) 56–66, https://doi.org/10.1107/S002188989300651X.
[46] C. Quaeyhaegens, G. Knuyt, L.M. Stals, Residual macroscopic stress in highly preferentially oriented titanium nitride coatings deposited on various steel types, J. Vacuum Sci. Technol. A: Vacuum Surfaces Films 14 (4) (1996) 2462–2469, https://doi.org/10.1116/1.580037.
[47] S.J. Skrzypek, A. Baczmański, W. Ratuszek, E. Kusior, New approach to stress analysis based on grazing-incidence X-ray diffraction, J. Appl. Crystallogr. 34 (4) (2001) 427–435, https://doi.org/10.1107/S0021889801005404.
[48] M. Marciszko, A. Baczmański, C. Braham, M. Wróbel, S. Wroński, G. Cios, Stress measurements by multi-reflection grazing-incidence X-ray diffraction method (MGIXD) using different radiation wavelengths and different incident angles, Acta Mater. 123 (2017) 157–166, https://doi.org/10.1016/j.actamat.2016.10.029.
[49] A. Oponowicz, M. Marciszko-Wiąckowska, A. Baczmański, M. Klaus, C. Genzel, S. Wroński, K. Kollbek, M. Wróbel, Gradient of Residual Stress and Lattice Parameter in Mechanically Polished Tungsten Measured Using Classical X-rays and Synchrotron Radiation, Metall Mater Trans A. 51 (11) (2020) 5945–5957.
[50] M. Marciszko, A. Baczmański, M. Klaus, C. Genzel, A. Oponowicz, S. Wroński, M. Wróbel, C. Braham, H. Sidhom, R. Wawszczak, A multireflection and multiwavelength residual stress determination method using energy dispersive diffraction, J. Appl. Crystallogr. 51 (2018) 732–745, https://doi.org/10.1107/S1600576718004193.
[51] P. Predecki, X. Zhu, B. Ballard, Proposed Methods for Depth Profiling of Residual Stresses using Grazing Incidence X-Ray Diffraction (GIXD), Adv. X-Ray Anal. 36 (1992) 237–245, https://doi.org/10.1154/S037603080001884X.
[52] C. Genzel, I.A. Denks, J. Gibmeier, M. Klaus, G. Wagener, The materials science synchrotron beamline EDDI for energy-dispersive diffraction analysis, Nucl. Inst. Meth. Phys. Res., A 1 (2007) 23–33, https://doi.org/10.1016/j.nima.2007.05.209.
[53] M. Klaus, C. Genzel, Reassessment of evaluation methods for the analysis of near-surface residual stress fields using energy-dispersive diffraction, J. Appl. Cryst. 52 (2019) 94–105, https://doi.org/10.1107/S1600576718018095.
[54] D. Apel, M. Meixner, A. Liehr, M. Klaus, S. Degener, G. Wagener, C. Franz, W. Zinn, C. Genzel, B. Scholtes, Residual stress analysis of energy-dispersive diffraction data using a two-detector setup: Part I — Theoretical concept, Nucl. Instrum. Methods Phys. Res., Sect. A 877 (2018) 24–33, https://doi.org/10.1016/j.nima.2017.09.005.
[55] B.C. Giessen, G.E. Gordon, X-ray Diffraction: New High-Speed Technique Based on X-ray Spectrography, Science 159 (1968) 973–975, https://doi.org/10.1126/science.159.3818.973-a.
[56] A. Baczmanski, A. Tidu, P. Lipiński, M. Humbert, K. Wierzbanowski, New Type of Diffraction Elastic Constants for Stress Determination, Mater. Sci. Forum 524–525 (2006) 235–240, https://doi.org/10.4028/www.scientific.net/MSF.524-525.235.

[57] W.H. Press, B.P. Flannery, S.A. Teukolsky, W.T. Vetterling, Numerical Recipes in C: The Art of Scientific Computing, second ed., Cambridge University Press, Cambridge, New York, 1992.
[58] H.-J. Bunge, Texture Analysis in Materials Science: Mathematical Methods, Butterworths and Co., London, 1982.
[59] M. Marciszko, A. Baczmański, M. Wróbel, W. Seiler, C. Braham, S. Wroński, R. Wawszczak, Problem of elastic anisotropy and stacking faults in stress analysis using multireflection grazing-incidence X-ray diffraction, J Appl Cryst. 48 (2) (2015) 492–509, https://doi.org/10.1107/S160057671500266610.1107/S1600576715002666/nb5129sup1.pdf.
[60] M. Marciszko, A. Baczmański, C. Braham, M. Wróbel, W. Seiler, S. Wroński, K. Berent, Analysis of stresses and crystal structure in the surface layer of hexagonal polycrystalline materials: a new methodology based on grazing incidence diffraction, J. Appl. Crystallogr. 49 (2016) 85–102, https://doi.org/10.1107/S1600576715021810.
[61] C.M. Brakman, T.H. de Keijser, N.M. van der Pers, P. Penning, S. Radelaar, Diffraction elastic constants for the determination of stresses in textured cubic materials: An experimental test, Philos. Mag. A 58 (4) (1988) 635–649, https://doi.org/10.1080/01418618808209942.
[62] C. Genzel, Evaluation of stress gradients ѝij(z) from their discrete laplace transforms ѝij(τk) obtained by x-ray diffraction performed in the scattered vector mode, Phys. Status Solidi (a). 156 (1996) 353–363, https://doi.org/10.1002/pssa.2211560213.
[63] M. Klaus, C. Genzel, X-ray residual stress analysis on multilayer systems: an approach for depth-resolved data evaluation, J. Appl. Cryst. 46 (2013) 1266–1276, https://doi.org/10.1107/S0021889813018517.
[64] M. Marciszko-Wiąckowska, A. Oponowicz, A. Baczmański, M. Wróbel, C. Braham, R. Wawszczak, Multireflection grazing-incidence X-ray diffraction: a new approach to experimental data analysis, J. Appl. Cryst. 52 (2019) 1409–1421, https://doi.org/10.1107/S1600576719013876.
[65] M. Marciszko, A. Baczmański, M. Wróbel, W. Seiler, C. Braham, J. Donges, M. Śniechowski, K. Wierzbanowski, Multireflection grazing incidence diffraction used for stress measurements in surface layers, Thin Solid Films 530 (2013) 81–84, https://doi.org/10.1016/j.tsf.2012.05.042.
[66] P. Thompson, D.E. Cox, J.B. Hastings, Rietveld refinement of Debye-Scherrer synchrotron X-ray data from Al2O3, J. Appl. Crystallogr. 20 (2) (1987) 79–83, https://doi.org/10.1107/S0021889887087090.
[67] M. Klaus, C. Genzel, J. García, Nondestructive separation of residual stress and composition gradients in thin films by angle- and energy-dispersive X-ray diffraction. II. Experimental validation, J. Appl. Cryst. 50 (2017) 265–277, https://doi.org/10.1107/S1600576716020604.
[68] T. Christiansen, M. Somers, Avoiding ghost stress on reconstruction of stress- and composition-depth profiles from destructive X-ray diffraction depth profiling, Mater. Sci. Eng., A 424 (2006) 181–189, https://doi.org/10.1016/j.msea.2006.03.007.
[69] K. Inal, P. Gergaud, M. François, J. Lebrun, X-ray diffraction methodologies of macro and pseudo-macro stress analysis in a textured duplex stainless steel, Scand. J. Metall. 28 (1999) 139–150.
[70] H. Dölle, The influence of multiaxial stress states, stress gradients and elastic anisotropy on the evaluation of (Residual) stresses by X-rays, J. Appl. Crystallogr. 12 (6) (1979) 489–501.
[71] M. Klaus, C. Genzel, Nondestructive separation of residual stress and composition gradients in thin films by angle- and energy-dispersive X-ray diffraction. I. Theoretical concepts, J. Appl. Cryst. 50 (2017) 252–264, https://doi.org/10.1107/S1600576716020598.
[72] M. Meixner, M. Klaus, C.h. Genzel, Sin2ψ-based residual stress gradient analysis by energy-dispersive synchrotron diffraction constrained by small gauge volumes. I. Theoretical concept, J. Appl. Cryst. 46 (3) (2013) 610–618, https://doi.org/10.1107/S0021889813008340.
[73] D. Apel, M. Klaus, M. Genzel, C. Genzel, Rietveld-based energy-dispersive residual stress evaluation: analysis of complex stress fields σ ij (z), J. Appl. Crystallogr. 47 (2014) 511–526, https://doi.org/10.1107/S1600576713034158.
[74] I.C. Noyan, Equilibrium conditions for the average stresses measured by X-rays, Metall. Mater. Trans. A 14 (9) (1983) 1907–1914, https://doi.org/10.1007/BF02645562.
[75] R. Wawszczak, A. Baczmański, M. Marciszko, M. Wróbel, T. Czeppe, K. Sztwiertnia, C. Braham, K. Berent, Evolution of microstructure and residual stress during annealing of austenitic and ferritic steels, Mater. Charact. 112 (2016) 238–251, https://doi.org/10.1016/j.matchar.2015.12.019.
[76] S. Wroński, A. Baczmański, R. Dakhlaoui, C. Braham, K. Wierzbanowski, E. C. Oliver, Determination of the stress field in textured duplex steel using the TOF neutron diffraction method, Acta Mater. 55 (18) (2007) 6219–6233, https://doi.org/10.1016/j.actamat.2007.07.044.
[77] A. Baczmański, M. Wroński, P. Kot, S. Wroński, A. Labaza, K. Wierzbanowski, A. Ludwik, M. Marciszko-Wic ackowska, The role of basal slip in the generation of intergranular stresses in magnesium alloy studied using X-ray diffraction and modelling, Mater. Design 202 (2021), https://doi.org/10.1016/j.matdes.2021.109543.
[78] E. Gadalińska, A. Baczmański, S. Wroński, L. Le Joncour, C. Braham, M. François, B. Panicaud, K. Wierzbanowski, Direct determination of phase stress evolution in duplex steel using synchrotron diffraction, Mater. Sci. Eng., A 801 (2021), 140400, https://doi.org/10.1016/j.msea.2020.140355.
[79] E. Gadalińska, A. Baczmański, C. Braham, G. Gonzalez, H. Sidhom, S. Wroński, T. Buslaps, K. Wierzbanowski, Stress localisation in lamellar cementite and ferrite during elastoplastic deformation of pearlitic steel studied using diffraction and modelling, Int. J. Plast. 127 (2020), 102651, https://doi.org/10.1016/j.ijplas.2019.102651.
[80] Y. Zhao, S. Wroński, A. Baczmański, L. Le Joncour, M. Marciszko, T. Tokarski, M. Wróbel, M. François, B. Panicaud, Micromechanical behaviour of a two-phase Ti alloy studied using grazing incidence diffraction and a self-consistent model, Acta Mater. 136 (2017) 402–414, https://doi.org/10.1016/j.actamat.2017.06.022.
[81] M. Wansleben, C. Zech, C. Streeck, J. Weser, C. Genzel, B. Beckhoff, R. Mainz, Photon flux determination of a liquid-metal jet X-ray source by means of photon scattering, J. Anal. At. Spectrom. 34 (7) (2019) 1497–1502, https://doi.org/10.1039/C9JA00127A.
[82] C. Genzel, M. Meixner, D. Apel, M. Boin, M. Klaus, Nondestructive residual stress depth profile analysis at the inner surface of small boreholes using energy-dispersive diffraction under laboratory conditions, J Appl Crystallogr. 54 (2021) 32–41, https://doi.org/10.1107/S1600576720014508.